

Dynamic evolution of competing same-dip double subduction: New perspectives of the Neo-Tethyan plate tectonics

Arnab Roy¹, Nibir Mandal¹, Jeroen Van Hunen²

¹High Pressure and Temperature Laboratory, Department of Geological Sciences,
Jadavpur University, Kolkata 700032, India.

²Department of Earth Sciences, Durham University, Durham, UK

Abstract

Same-dip double-subduction (SDDS) systems are widely reported from present as well as past complex convergent plate tectonic configurations. However, the dynamics of their evolution is poorly understood, which is crucial to conceptualize anomalous subducting slab kinematics and associated observed geological phenomena, such as irregular trench migration rates, high convergence velocities, and slab break-off. To bridge this gap, we develop dynamic thermo-mechanical subduction models and investigate the initiation and evolution of SDDS systems, considering three different initial plate configurations: oceanic, oceanic-continental and multiple continental settings, based on Neo-Tethyan paleo-reconstructions. Each model offers new insights into the complex tectonic history of the major Neo-Tethyan subduction zones, particularly the Indo-Eurasian and Andaman convergent systems. We evaluate the slab-slab interactions, trench and subduction kinematics, inter-plate reorganization, and temporally varying mantle flow patterns involved in the dynamic evolution of these SDDS systems. The oceanic SDDS model simulations reveal that a sizable oceanic plate can initiate two subduction zones synchronously, and they evolve unequally in a competing mode, leading to exceptionally high convergence rates (~16-17 cm/year) for a prolonged duration (~7-8 Myr). This finding explains the coeval activity of coupled subduction zones in the Indo-Eurasia convergence during the Cretaceous evolution of the Neo-Tethys. We further implement a corresponding single subduction model to assess the additional effects of competing slab kinematics in an oceanic SDDS setting. The ocean-continent SDDS model, on the other hand, localizes subduction preferentially at passive margins between the oceanic plate and the continental block, forming double subduction zones that grow almost equally to form a spreading centre between the two trenches. These model results allow to reconstruct the Cenozoic evolution of the eastern Neo-Tethyan region, which ultimately led to the development of the Andaman subduction zone. We also show the post-Cretaceous evolution of the Indo-Eurasian collision zone as a consequence of the SDDS dynamics in presence of multiple continental blocks. These dynamics facilitated slab break-off, transforming the SDDS into a single subduction system in a relatively short time frame (~3 Myr). We finish with a synthesis of the paleo-reconstructions of the Neo-Tethys in the perspective of these SDDS models.

Keywords: Convergent plate tectonics, double subduction systems, dynamic subduction modelling, Finite element method, slab interaction, spreading centre locations, tectonic evolution of Neo-Tethys

1. Introduction

Subduction zones are spectacular planetary-scale manifestations of the convergent plate tectonics, and govern a wide range of geological phenomena, such as continental crust formation, magmatism and geochemical recycling, and geophysical processes, such as earthquake localization and energy dissipation (Corbi et al., 2017; Stern, 2002; Tilling, 1996). Subduction tectonics often turn complicated due to complex configurations of multiple plates, kinematically linked with one another. Double subduction systems are a common example of such convergent settings, where two lithospheric slabs subduct synchronously along sub-parallel trenches (Fig. 1). They are widely reported from the present-day plate configurations (Fig. 1), e.g., the Mediterranean (Király et al., 2018; Vignaroli et al., 2008), the Molucca Sea (Zhang et al., 2017), Taiwan (Lin and Kuo, 2016), New Zealand (Lamb, 2015), and around the Philippines plate

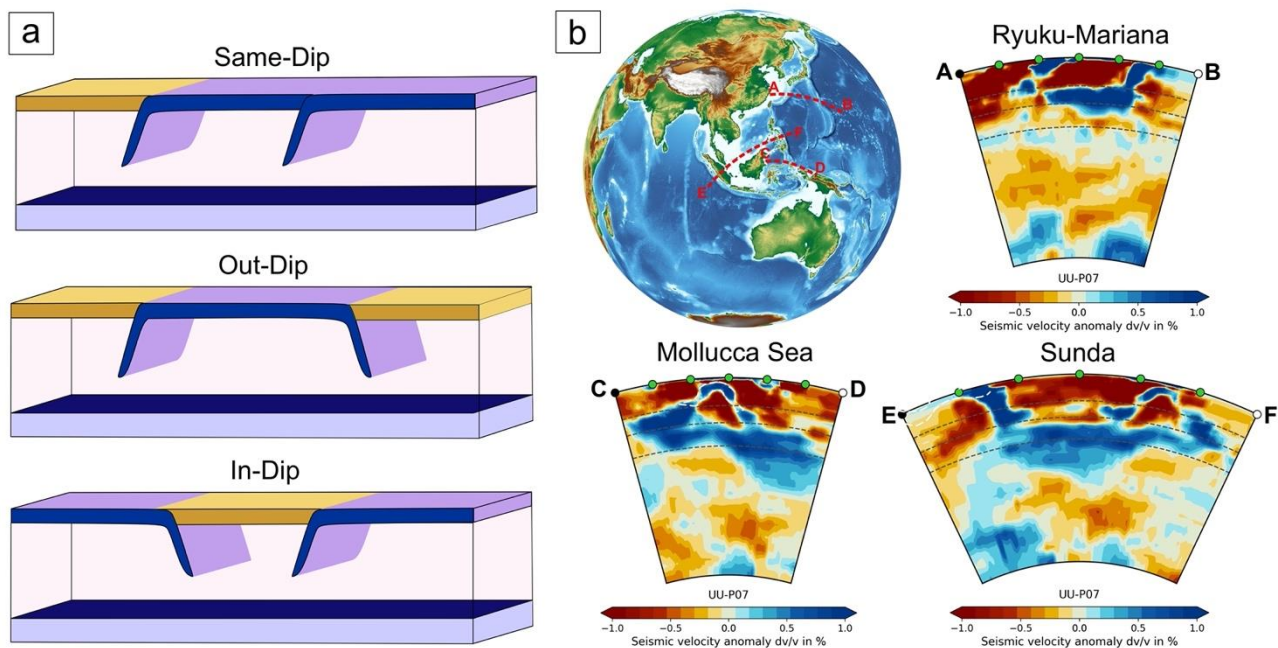


Figure 1: Illustrations showing a) the three different types of double subduction systems and b) their natural counterparts observed from seismic tomography. The P-wave model used for this analysis is UU-P07 (Amaru, 2007).

1
2
3
4 43 (Ryukyu vs. Izu-Bonin-Mariana trenches; (Faccenna et al., 2018; Hall and Spakman, 2002)), as
5
6 44 well as from paleo-reconstructions, e.g., Trans-Tethyan System (Jagoutz et al., 2015), and Late
7
8
9 45 Cretaceous eastern Turkey evolution (Eyuboglu et al., 2019). The double-subduction model has
10
11 46 recently received much attention to address the problem of enigmatic slab kinematics encountered
12
13
14 47 at both modern and ancient convergent zones (Čížková and Bina, 2015; Dasgupta and Mandal,
15
16 48 2018; Jagoutz et al., 2015). Based on seismic tomography and available plate kinematics data from
17
18
19 49 GPS observations, three types of double-subduction configurations (Király et al., 2021) have been
20
21 50 recognized: outward-, inward- and same-dipping slabs (Fig. 1). This study, however, explores the
22
23
24 51 complex dynamics of same-dip double subduction with a focus on the Neo-Tethyan tectonic
25
26 52 evolution.

27
28
29 53 Plate reconstruction studies suggest that same-dip double subduction (SDDS) systems
30
31 54 developed repeatedly in the course of the ~150 Myr Neo-Tethyan evolutionary history (Hall, 2012;
32
33 55 Kufner et al., 2016; Pusok and Stegman, 2020). Using quantitative models, Jagoutz et al. (2015)
34
35
36 56 have shown the existence of coupled subduction zones in the Trans-Tethyan intra-oceanic system
37
38 57 below the southern margin of Eurasia. During the Cretaceous to Early Tertiary period, this tectonic
39
40
41 58 system evolved through multiple Neo-Tethyan subduction episodes, featuring the Kshiroda Plate's
42
43 59 north-dipping oceanic slab under Eurasia (Yin and Harrison, 2000) and intra-oceanic subduction
44
45
46 60 of the northern oceanic segment of the Indian subcontinent beneath the Kshiroda Plate leading to
47
48 61 the formation of the Kohistan extensional arc. Geological, geochemical, and paleomagnetic
49
50
51 62 investigations in the tectonic units, specifically the forearc, oceanic melange, and ophiolite
52
53 63 sequences of the Himalayas (Aitchison et al., 2000; Bouilhol et al., 2013; Hall, 2012; Yin and
54
55 64 Harrison, 2000) imply the concurrence of parallel subduction zones with similar dipping
56
57
58 65 orientations. Complementing these findings, geophysical observations, such as the detection of
59
60
61
62
63
64
65

1
2
3
4 66 multiple slab remnants through seismic tomography models (Van Der Voo et al., 1999), and
5
6 67 alterations in trench kinematics and the upper plate's deformation patterns (Gürer et al., 2016;
7
8
9 68 Jolivet et al., 2018), further reinforce the argument in favour of SDDS. Similarly, recent works
10
11 69 have recognized multiple double-subduction events to reconstruct the evolution of the Andaman
12
13
14 70 Subduction system (Advokaat et al., 2018; Bandyopadhyay et al., 2020; Ghosh et al., 2017). Its
15
16 71 active tectonics now occurs at the northern flank of the Java trench where the oceanic part of the
17
18
19 72 Indian Plate subducts at a low angle to the arc-trend beneath the overriding Andaman
20
21 73 microcontinental block. Geochronological correlations and geochemical signatures of the arc-
22
23
24 74 volcanism (Westerweel et al., 2019) and ophiolitic suites (Acharyya et al., 1991) indicate the
25
26 75 activity of a second subduction zone on the eastern side in late-Miocene, continuing to present day.
27
28
29 76 Also, geochemical evidence (Ghosh et al. 2017) suggests that the Andaman-Nicobar outer-arc high
30
31 77 grew from the coalescence of two accretionary prisms linked to the double-subduction tectonics.
32
33
34 78 Despite a significant advancement of their geochemical and geophysical information, there
35
36 79 remains a necessity of dynamically self-consistent geodynamic models to conceptualize the
37
38
39 80 following unresolved tectonic issues of these SDDS systems: 1) the unusually high Late
40
41 81 Cretaceous Indo-Eurasian subduction velocity, although the Kohistan extensional zone reduced
42
43 82 the transfer of pull force from front to rear slab, 2) reconstruction of the Andaman Convergent
44
45
46 83 System in the framework of Neo-Tethyan tectonics, and 3) dynamic backdrop of the failed trench
47
48 84 at Amirante and its relationship to the Cenozoic Indo-Eurasian subduction. This study aims to
49
50
51 85 develop SDDS models, mainly to address these long-standing issues of the Neo-Tethyan tectonics.

52
53 86 Recent analogue and numerical modelling have dealt with the complexities in double-
54
55 87 subduction evolution and their effects on the regional plate motion, intraplate deformations, slab
56
57
58 88 interactions and topographic developments (Dasgupta and Mandal, 2018; Holt et al., 2017; Király
59
60
61
62
63
64
65

1
2
3
4 89 et al., 2021; Mishin et al., 2008; Peral et al., 2018; Pusok and Stegman, 2019). It is now a well-
5
6 90 established fact that their mode of development significantly differs from that of a single-
7
8 91 subduction system. The additional complexity originates primarily from inter-slab interactions that
9
10 92 greatly influence the plate bending and viscous dissipation in the mantle, coupled with additional
11
12 93 factors, such as contrasting plate ages, plate dimensions, rheology, and inter-slab distance (Čížková
13
14 94 and Bina, 2015; Dasgupta and Mandal, 2018; Holt et al., 2017). The initial relative arrangement
15
16 95 of tectonic plates is another influential factor in the double-subduction evolution. For instance,
17
18 96 the Ryukyu-IBM system has an intra-oceanic subduction zone coupled with another subduction
19
20 97 zone at an ocean-continent convergence boundary. In contrast, the Trans-Tethyan double
21
22 98 subduction formed with the Indian continental plate linked to the subducting oceanic counterpart.
23
24 99 This difference in the initial plate arrangements might have led to their contrasting evolutionary
25
26 100 paths, resulting in completely different tectonic histories of these two regions. However, how the
27
28 101 initial plate configuration governs the dynamic evolution of a SDDS system is still an open-ended
29
30 102 question, which the present article addresses in the context of the Neo-Tethyan subduction
31
32 103 tectonics.

33
34 104 We develop geodynamic models to simulate the thermo-mechanical evolution of SDDS
35
36 105 systems, initiated along pre-existing lithospheric weaknesses and reconstruct the tectonic history
37
38 106 of both the Indo-Eurasian and Andaman double subduction systems. The models are designed to
39
40 107 reproduce time-dependent and self-consistently evolving subduction for a given plate
41
42 108 configuration. This modelling allows to address the following key questions: 1) can two adjacent
43
44 109 same-dip subduction zones grow concurrently, and 2) if so, how do these neighbouring subduction
45
46 110 zones mutually influence each other during their evolution, depending on their initial tectonic
47
48 111 configurations? We also explore the following influential phenomena: a) mutual interactions of
49
50
51
52
53
54
55
56
57
58
59
60
61
62
63
64
65

1
2
3
4 112 simultaneous subducting-slab motions during the evolution of commonly reported Neo-Tethyan
5
6 113 SDDS systems, b) complexity in the associated mantle flow patterns and their role in localization
7
8
9 114 of lithospheric-scale extensional zones in convergent tectonics, and c) slab detachment leading to
10
11 115 a double- to single-subduction transition.
12
13

15 116 **2. Numerical Modelling Approach**

18 117 *2.1. Model Design*

21 118 We use 2D thermomechanical numerical models (Fig. 2) that are inherently dynamic, implying
22
23 119 that no external forces or velocities are applied to the overall system. Details of the numerical
24
25 120 method and model boundary conditions are provided in Appendix A. The model domain represents
26
27 121 a rectangular 7000 km (horizontal) x 1000 km (depth) vertical section (Fig. 2a). We introduce
28
29 122 mechanical weaknesses in the lithospheric layer, as considered in previous studies that suggested
30
31 123 spontaneous subduction initiation to occur preferentially at the locations of pre-existing
32
33 124 lithospheric weakness, e.g., transform faults (Arcay et al., 2020; Zhou et al., 2018). This weak-
34
35 125 zone perturbation for subduction initiation is a viable mechanical model in the light of damage
36
37 126 theory proposed by Bercovici & Ricard, 2014. Our model implements this weakness as a narrow
38
39 127 (10 km wide), low-viscosity (10^{20} Pa s) zone, extending to the lithospheric base (Fig. 2). The weak
40
41 128 zones can also characterize intraplate lithosphere-scale faults in large oceanic plates, like the
42
43
44
45
46
47
48
49
50
51
52
53
54
55
56
57
58
59
60
61
62
63
64
65

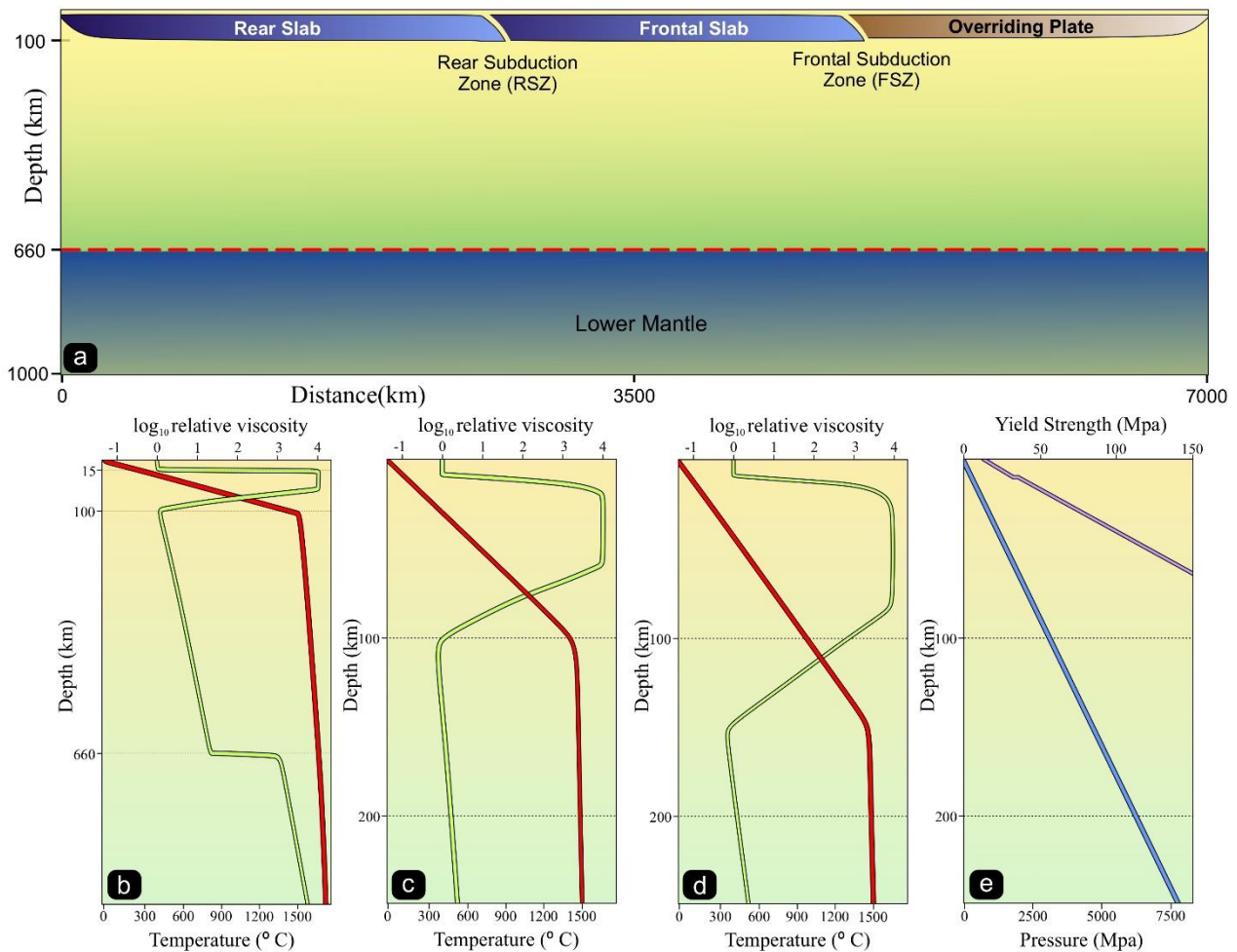


Figure 2: (a) The model setup and boundary conditions considered for CFD simulations, which shows the whole domain and initial setup of model employed for simulating same-dip double subduction in oceanic setting. Detailed illustrations representing the viscosity and temperature profiles of b) the complete model domain, c) oceanic lithosphere, and d) continental lithosphere utilized in the models. The viscosity values are relative to the asthenosphere value of 10^{20} Pa s. e) The strength plots exhibiting depth-dependent variations, showcasing increasing strength (purple) and pressure (blue).

129 present-day Wharton Basin (Stevens et al., 2020). All the rheological and thermal parameters used

130 in this study are summarized in Table 1.

131 2.2. Model Configurations

132 Natural subduction zones occur in various convergent settings, which can be broadly
 133 categorized as: 1) oceanic settings (e.g., Izu-Bonin-Mariana), where two or more oceanic plates
 134 converge to each other; 2) ocean – continent settings (e.g., the Andean subduction system), where
 135 oceanic plates converge against continents; and 3) continent-continent settings (e.g. the Indo-

1
2
3
4 136 Eurasia collisional zone), where two or more continents approach each other. Considering Earth's
5
6 137 present-day plate structures, SDDS systems can develop in any of these three tectonic settings,
7
8
9 138 giving rise to a spectrum of their potential plate configurations. Based on the paleo-reconstructions
10
11 139 of the Neo-Tethyan tectonics, we thus chose three different cases for the model settings, with an
12
13
14 140 objective to investigate the mode of double-subduction evolution depending on the initial plate
15
16 141 architecture. Each of these initial settings accounts for local lithospheric weaknesses in a specific
17
18
19 142 arrangement with or without mechanically strong continental blocks.
20

21 143 The first case of our subduction modelling (referred to as *oceanic plate model*) replicates a
22
23 144 simple oceanic plate tectonic setting, consisting of a 120 Myr old, flat lying oceanic lithosphere
24
25
26 145 with a length of 5000 km (Fig. 3a). The model initially contains two similarly-dipping narrow
27
28
29 146 weak zones of different thicknesses in the oceanic lithospheric plates at distances of 2500 km and
30
31 147 5000 km. The weak-zone configuration is chosen so that the model favours one of the weak zones
32
33 148 to become active first to initiate an ocean-ocean subduction zone, as reported from natural SDDS,
34
35
36 149 such as the Trans-Tethyan subduction system. No continent is included in the model domain to
37
38 150 exclusively show the effects of oceanic plates on the SDDS dynamics. We also implement a
39
40
41 151 corresponding single subduction model (Supplementary section S1) to find the additional effects
42
43 152 of inter-slab interactions. The second case (referred to as *oceanic– continental plate model*) is
44
45
46 153 designed to represent an ongoing subduction system, where an oceanic plate has already been
47
48 154 subducted into the upper mantle, carrying a 400 km long and ~150 km thick microcontinental
49
50
51 155 block (Fig. 4a). This configuration aims to reveal the mechanical effects of pre-existing micro-
52
53 156 continent between two oceanic plates. The continental crust is assigned a compositional density
54
55 157 lower than that of mantle material by 600 kg/m^3 . The block is assumed to form a weak interface
56
57
58 158 with the adjoining oceanic plate, possibly resulting from the inter-plate 3D differential stress
59
60
61
62
63
64
65

1
2
3
4 159 localization (Auzemery et al., 2020; Heidbach et al., 2007). On the rear side, it is separated from
5
6
7 160 an 80 Ma old oceanic lithosphere by a dipping (30°) weak zone. The third model, designed to
8
9 161 reproduce a continent-continent collisional setting (referred to as *multiple continent model*),
10
11 162 initially consists of a flat-lying 1200 km long, 80 Myr old oceanic lithosphere, and two continental
12
13 163 blocks (thickness: 150 km and length: 1500 km), separated by an oceanic basin. This oceanic plate
14
15 164 forms a narrow weak channel at the contact with the overriding strong continental plate (Fig. 5a).
16
17
18
19 165 The continental blocks are compositionally buoyant relative to the underlying asthenosphere.
20

21 166 **3. Model results**

22 167 *3.1. Oceanic plate settings*

23
24 168 This model setting localizes plastic yielding preferentially at one of the pre-existing
25
26
27 169 lithospheric weaknesses (Fig.3a), resulting in an unstable state of the flat-lying oceanic plate to
28
29
30 170 initiate the rear subduction zone (RSZ). This process accompanies the formation of a divergent
31
32
33 171 spreading centre that eventually acts as an active site of oceanic plate generation. At ~ 6 Myr, the
34
35
36 172 newly generated lithosphere constitutes a well-developed overriding plate (OP) structure in the
37
38
39 173 subduction zone. The proto-slab subducts to a depth of ~ 300 km with a convergence rate (V_C) of
40
41
42 174 ~ 13 cm/yr (relative to its adjoining overriding oceanic plate) at 8.1 Myr (Fig 3b). The active RSZ
43
44 175 plate approaches the trench with a velocity (V_P) of $\sim +12$ cm/year (+ sign denotes movement
45
46
47 176 towards the right), while the trench itself retreats with a velocity (V_{RT}) of ~ -2.5 cm/yr. The plate
48
49 177 convergence velocity (calculated between passive markers 1 and 3; Fig. 3a) accelerates further
50
51
52 178 with increasing total negative buoyancy to attain a maximum value of ~ 15 cm/year (Fig. 6a), and
53
54 179 the RSZ slab dip (measured at 125 km depth) steepens to $\sim 45^\circ$. The slab subsequently encounters
55
56
57 180 the 660-km transition at 10.1 Myr, and decelerates ($V_P \approx 7.5$ cm/yr) due to higher viscous resistance
58
59
60
61
62
63
64
65

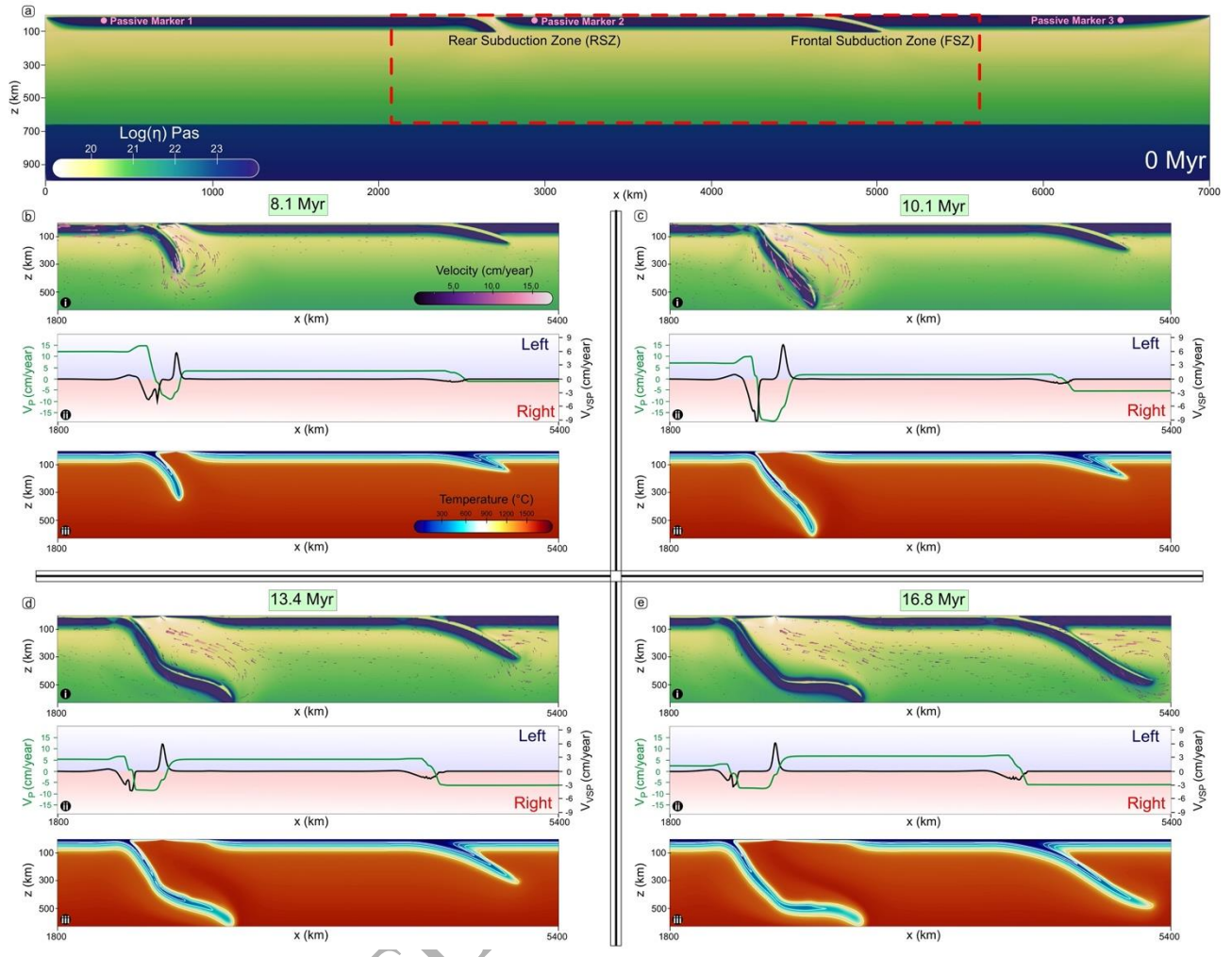


Figure 3: Evolution of the double subduction model in an oceanic setting. Panels show: (a) the initial viscosity field of the complete numerical model domain, (b)-(e) evolution of the i) viscosity and velocity fields, ii) plate velocities (V_P) (green) and vertical subduction-velocity (V_{VSP}) (black), which denote the horizontal (V_x) and vertical (V_y) component of the total velocity vector respectively, and iii) temperature field, zoomed into a region around the subduction zone for four time-steps corresponding to the back subduction initiation ($t= 8.1$ Ma), frontal subduction initiation ($t= 10.1$ Ma), frontal subduction free sinking ($t= 13.4$ Ma) and mature double subduction ($t= 16.8$ Ma) phases.

181 in the stronger lower mantle. This slab-lower mantle interaction also forces the oceanic plate to
 182 slow down its motion ($V_c \approx 12$ cm/year; Fig. 6a), prompting the other proto-slab to activate and
 183 initiate the frontal subduction zone (FSZ) (Fig. 3c). At this stage, the tectonic setting transforms
 184 into a typical double-subduction configuration, albeit with significant asymmetry in terms of both
 185 slab geometry and kinematics, where the FSZ slab shows much shallower dip ($\sim 20^\circ$) and lower
 186 convergence velocity ($V_c^{RS} \approx 7$ cm/yr) than the rear subducting slab. Additionally, the RSZ trench

1
2
3
4 187 retreats significantly faster ($V_{RT} \approx 9$ cm/yr) than the FSZ trench ($V_{FT} \approx 2.5$ cm/yr). The cumulative
5
6
7 188 effects of double-subduction motion facilitate the convergence motion to not only attain, but also
8
9 189 sustain extremely high velocities for a prolonged period (~ 6 Myr). This is in stark contrast to
10
11
12 190 scenarios of single subduction, where such extreme convergence rates can prevail over short
13
14 191 durations (< 1 Myr).

15
16 192 The double-subduction system always maintains an active state of the spreading centre to
17
18
19 193 continuously produce new lithospheric materials. At ~ 13.4 Myr, the RSZ attains a declining stage,
20
21 194 marked by a significant drop in V_P (~ 5 cm/yr), although its trench continues to retreat with $V_{RT} \sim 3$
22
23 195 cm/yr. In contrast, the FSZ continues to remain active, with its slab sinking rapidly into the upper
24
25
26 196 mantle to facilitate the convergence velocity ($V_P \approx 5$ cm/year) as well as the trench retreat velocity
27
28 197 ($V_{FT} \approx 7$ cm/year). However, the SDDS system cumulatively shows a decreasing trend of the net
29
30
31 198 convergence velocity ($V_c \approx 11$ cm/yr). At ~ 16.8 Myr, the rear subducting slab moves backward as
32
33 199 V_{RT} (~ 3.5 cm/year) exceeds V_P (~ 2.5 cm/year) and the double-subduction evolves to a steady state
34
35
36 200 condition of the RSZ in terms of V_c and slab dip ($\sim 55^\circ$). On the opposite side, however, the oceanic
37
38 201 plate associated with the FSZ acquires a maximum velocity $V_P \approx 6.5$ cm/year, significantly higher
39
40
41 202 than the rear subducting plate velocity. The FSZ slab then moves through the entire upper mantle
42
43 203 to encounter the lower mantle and eventually slows down its velocity. The corresponding trench
44
45
46 204 continues to retreat with $V_{FT} \approx 6$ cm/yr, which subsequently surpasses the FSZ plate velocity in
47
48 205 course of the subduction evolution (> 20 Myr). The convergence attains a velocity of ~ 8.5 cm/year
49
50
51 206 with a tectonically-steady configuration till the end of the model run.

52
53 207 During the RSZ-initiation stage, the descending-slab driven mantle flows exhibit both
54
55 208 vertical and horizontal components, shaping a circulating flow vortex around the subducted slab.
56
57
58 209 The vortex remains active till ~ 10 Ma, gradually waning as the RSZ slab decelerates upon
59
60
61
62
63
64
65

1
2
3
4
5
6
7
8
9
10
11
12
13
14
15
16
17
18
19
20
21
22
23
24
25
26
27
28
29
30
31
32
33
34
35
36
37
38
39
40
41
42
43
44
45
46
47
48
49
50
51
52
53
54
55
56
57
58
59
60
61
62
63
64
65

encountering the 660 km discontinuity. With this deceleration, the vortex's focal point shifts to the FSZ slab, accompanied by an increasing flow intensity with time. At ~13 Myr, the double-subduction configuration sets in a potent upward slab-parallel flow beneath the spreading centre, which strengthens further by merging with the counter-flow generated by the frontal subducting slab (Fig. 3e-i). Together, these components constitute a robust mechanism for channelling mantle materials towards the spreading centre. Notably distinct from typical single-subduction driven corner and wedge flows, this increased mantle-material supply emerges as a pivotal factor to facilitate the accretion rates of lithosphere.

3.2. *Microcontinent - oceanic plate setting*

The micro-continent-bearing oceanic plate setting consists of an already initiated subduction in the front (FSZ: frontal subduction zone) and the lithospheric weakness between the microcontinent. This configuration results in initiation of the rear subduction zone, forming a double-subduction system at an early stage (~6 Myr) of the model run (Fig.4b), as evident from a convergence velocity $V_C \approx 5$ cm/yr (Fig. 6b). The subduction zones, however, grow at different rates, where the FSZ subduction is much more active than the RSZ. This difference in their subduction rates causes rifting between the FSZ oceanic plate and the microcontinent. The rift subsequently acts as a spreading centre, allowing upwelling of the underlying mantle material to the surface and generate new oceanic lithosphere between the continental and the frontal oceanic

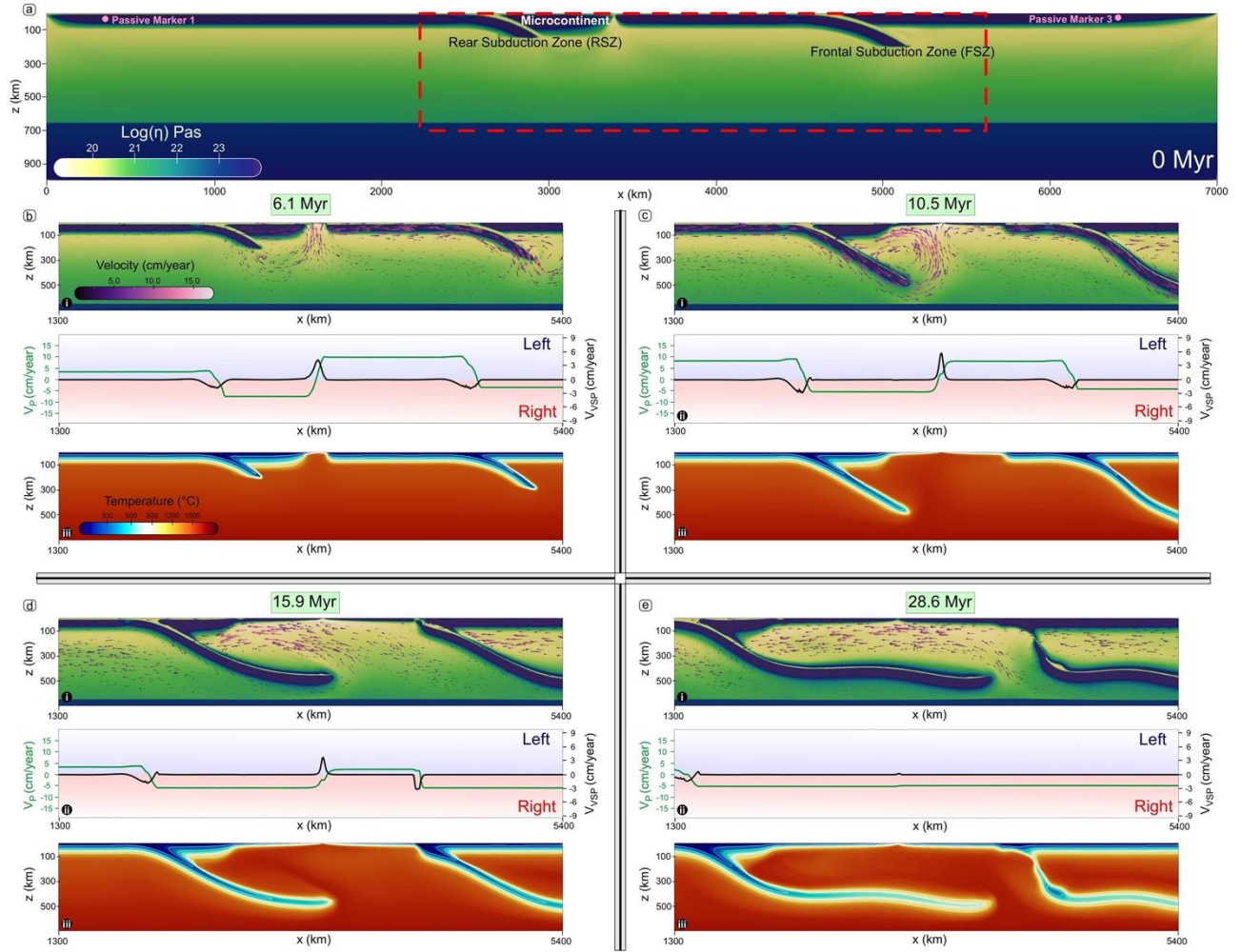


Figure 4: Evolution of the double subduction model in presence of a continental block. Panels show: (a) the initial viscosity field of the complete numerical model domain, (b)-(e) evolution of the i) viscosity and velocity fields, ii) plate velocities (V_P) (green) and vertical subduction-velocity (V_{VSP}) (black), which denote the horizontal (V_x) and vertical (V_y) component of the total velocity vector respectively, (see Supplementary section S2) and iii) temperature field, zoomed into a region around the subduction zone for four time-steps corresponding to the fore subduction free sinking ($t = 6.1$ Ma), back subduction free sinking ($t = 10.5$ Ma), mature double subduction ($t = 15.9$ Ma) and fore subducting slab detachment ($t = 28.6$ Ma) phases.

At ~ 6.1 Myr, the RSZ proto-slab subducts to a depth of ~ 200 km into the upper mantle, and this subduction motion forces the continental block to act as an OP, moving trench-ward at a velocity $V_P \sim -7$ cm/year. The FSZ slab, on the other side, continues to subduct freely into the upper mantle, setting the entire plate to move at a high velocity ($V_P \sim +10$ cm/yr) (Fig. 4a). During this phase of tectonic evolution both the trenches retreat, but with contrasting velocities; the RSZ trench

1
2
3
4 233 retreats at a significantly faster rate ($V_{RT} \approx -6.5$ cm/yr) than the FSZ ($V_{FT} \approx -3.8$ cm/yr). The
5
6 234 convergence velocity between the main OP and the RSZ slab is ≈ 7 cm/year, which increases to a
7
8
9 235 high value ($V_C \approx 13$ cm/yr) on a model run time of ~ 9 Myr (Fig. 6b). The frontal oceanic slab
10
11 236 reaches the lower mantle at ~ 10.5 Myr and begins to slow down the velocity ($V_P \approx +7$ cm/yr) due
12
13
14 237 to higher viscous forces in the 660-km transition zone. The RSZ slab, however, continues to
15
16 238 subduct through the upper mantle and maintains the rear oceanic plate movement at a velocity of
17
18
19 239 $\approx +8$ cm/year. The RSZ trench at the same time retreats, but with a reduced velocity ($V_{RT} \approx -5$
20
21 240 cm/yr), whereas the FSZ trench continues to retreat at a steady rate ($V_{FT} \approx -4$ cm/year). The
22
23
24 241 convergence velocity is high ($V_C \approx 13$ cm/year), but shows a diminishing trend after this period. At
25
26 242 ~ 15.9 Myr, both the subducting oceanic slabs lower their dips to become almost flat, and
27
28
29 243 significantly reduce the plate velocities ($V_P \approx +2.5$ cm/yr and $\approx +3.5$ cm/yr for FSZ and RSZ slabs,
30
31 244 respectively). The relatively buoyant juvenile (~ 15 Myr) lithosphere, formed at the spreading
32
33 245 centre, eventually reaches the FSZ trench and its subduction accelerates the retreat motion (V_{FT}
34
35
36 246 $\approx +7.5$ cm/year). This motion reduces its slab dip from 30° to $\sim 26^\circ$ (Fig. 6b), which starts to
37
38 247 increase significantly after ~ 18 Myr. The RSZ trench retreat velocity (V_{RT}) increases to -5.5 cm/yr
39
40
41 248 during this period. At ~ 25 Myr, the FSZ slab undergoes break-off at the location of maximum
42
43 249 strain localisation developed by the negative buoyancy induced slab pull (see Supplementary S3
44
45
46 250 for detailed strain-rate plots).

47
48 251 In this SDDS system, the spreading centre located between the two trenches remains active,
49
50 252 continuously adding new lithosphere to accommodate the increasing space between the continental
51
52
53 253 block and the frontal oceanic plate. At ~ 28.6 Myr, the spreading centre, however, becomes almost
54
55
56 254 inactive as the upwelling process is replaced by slab-driven horizontal flows in the mantle region
57
58 255 between the two subducting plates. The entire newly formed lithosphere is coherently coupled with
59
60
61
62
63
64
65

1
2
3
4 256 the main OP, as revealed from the plate velocity ($V_P \approx -5$ cm/year). The double subduction system
5
6
7 257 ceases to exist due to the absence of slab pull force at the FSZ trench and transforms into a single
8
9 258 subduction system.

12 259 *3.3. Multiple-continental plate setting*

14 260 The model run shows that subduction localizes preferentially along the lithospheric
15
16
17 261 weakness to initiate the frontal subduction zone (FSZ), leaving the trailing weak zone at the
18
19 262 continent-oceanic plate interface almost inactive (Fig. 5b). At this stage (~ 4 Myr) the system
20
21
22 263 follows mostly single-subduction dynamics, allowing the FSZ slab to penetrate into the upper
23
24 264 mantle to a depth of ~ 200 km. The plate velocity (V_P) increases to $\sim +7.5$ cm/year on a model run
25
26
27 265 time of 8.5 Myr (Fig. 5b). The velocity field indicates that the lithospheric plates move coherently
28
29 266 as a single unit to subduct beneath the FSZ trench although a lithospheric weakness is present in
30
31
32 267 between them ($V_P \approx +5$ cm/year for rear oceanic plate). This implies that the FSZ entirely
33
34 268 determines the dynamics of the system at an early stage. The frontal oceanic plate progressively
35
36 269 accelerates its motion to attain a convergence rate ($V_c^{RS} \approx 8$ cm/year, Fig. 6c solid blue line) with
37
38
39 270 respect to the OP at ~ 11.5 Myr. At this stage the subduction system undergoes a remarkable
40
41 271 kinematic transformation, leading to plate decoupling at the rear lithospheric weakness that
42
43
44 272 eventually triggers mantle upwelling and accretion of new lithospheric materials to form a thin
45
46 273 overriding plate. This decoupling decelerates the rear plate motion ($V_P \approx +1$ cm/year) and brings it
47
48
49 274 almost to a halt. In contrast, the frontal slab continues to maintain a high plate velocity ($V_P \approx +7.5$
50
51 275 cm/year) and a high convergence rate ($V_c^{RS} = +7.5$ cm/year), along with a moderate trench retreat
52
53
54 276 rate ($V_{FT} \approx -3.5$ cm/yr). At ~ 12.5 Myr, the rear subducting slab gains a significant slab-pull velocity
55
56 277 ($V_{SP} \approx -10$ cm/year), which consequently causes initiation of the rear subduction zone (RSZ). The
57
58
59 278 proto-slab continues to move through the upper mantle, setting the convergence velocity rapidly
60
61
62
63
64
65

279 accelerate to attain a value of ~ 11 cm/year at 13.8 Myr. On the other side, the FSZ slab reaches the
 280 660-km transition zone and slows down its overall sinking velocities. The continental block in this
 281 plate reaches the trench and collides with the overriding plate, switching a reversal in the trench
 282 motion to advance at a rate $V_{FT} \approx +2$ cm/yr. The collision event also reduces the plate velocity (V_P
 283 $\approx +5$ cm/yr) as well as the convergent velocity ($V_c^{RS} \approx 4.5$ cm/yr) at ~ 15 Myr. Eventually, the RSZ
 284 experiences strong extensional forcing created by the FSZ, and its convergence reduces to

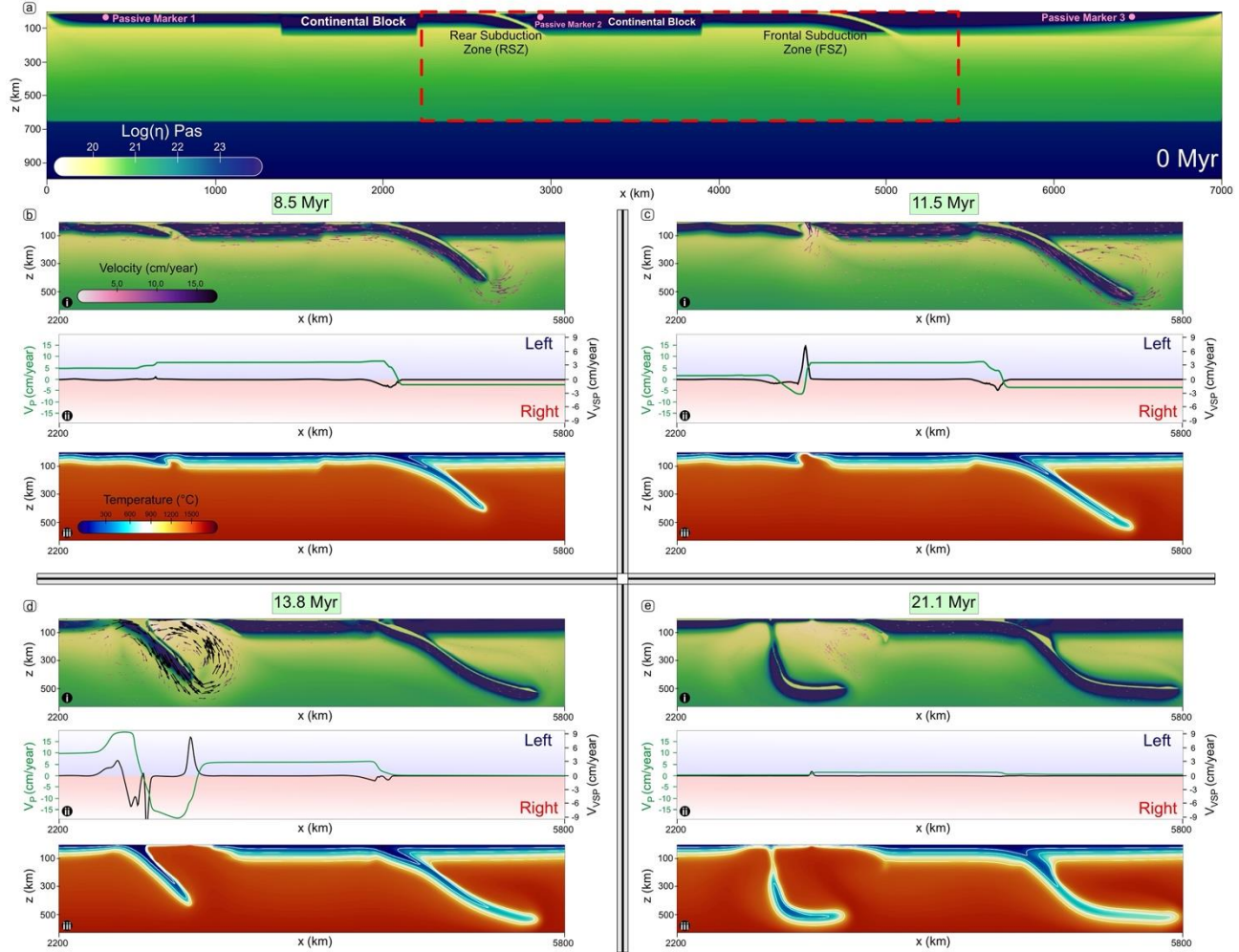
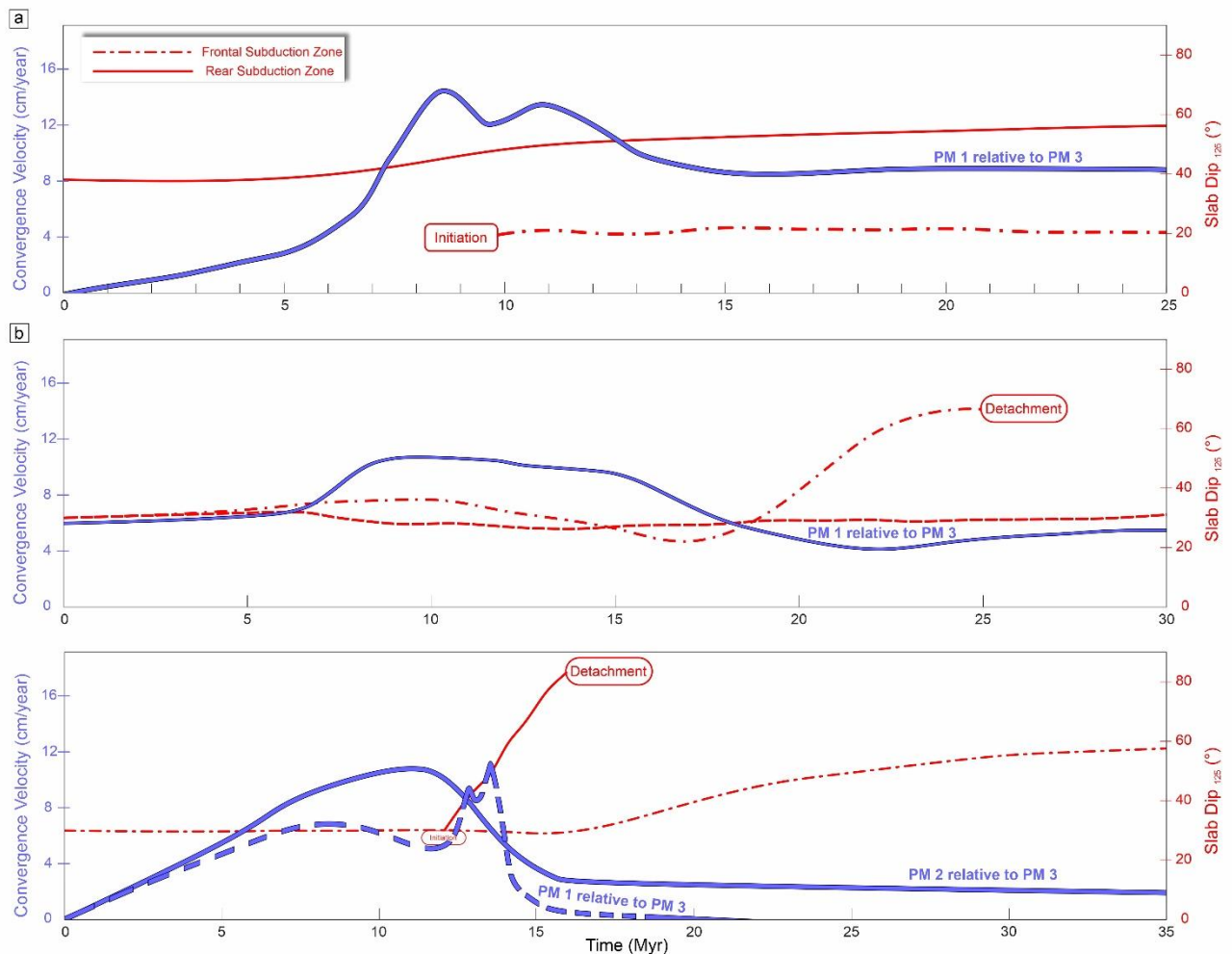


Figure 5: Evolution of the double subduction model in presence of multiple continental plates. Panels show: (a) the initial viscosity field of the complete numerical model domain, (b)-(e) evolution of the i) viscosity and velocity fields, ii) plate velocities (V_P) (green) and vertical subduction-velocity (V_{VSP}) (black), which denote the horizontal (V_x) and vertical (V_y) component of the total velocity vector respectively, and iii) temperature field, zoomed into a region around the subduction zone for four time-steps corresponding to the fore subduction free sinking ($t = 8.5$ Ma), continental collision ($t = 11.5$ Ma), back subduction initiation ($t = 13.8$ Ma) and back subducting slab detachment ($t = 21.1$ Ma) phases.

1
2
3
4 285 extremely low rates, which impedes the trench retreat, causing the RSZ slab to steepen ($>65^\circ$) and
5
6
7 286 eventually break off. The continental block plays an instrumental role to facilitate triggering the
8
9 287 slab detachment at ~ 16 Myr. In course of the double-subduction evolution (~ 21.1 Myr), the plate
10
11 288 velocities drastically drop to ~ 2.5 cm/year and the tectonic setting transforms into a single
12
13
14 289 subduction system. Thus, these results show that in this SDDS system, two simultaneous
15
16 290 subduction zones cannot be sustained and the subduction behind the collision zone ceases without
17
18
19 291 attaining maturity.



54
55 Figure 6: Temporal evolution of subduction zone convergence rates and shallow slab dips (at depth = 125 km)
56 of fore and back subducting slabs, for double subduction in a) oceanic setting, b) microcontinent - oceanic
57 plate setting and, c) multiple continental plate setting. PM: Passive Marker
58
59
60
61
62
63
64
65

292 4. Discussion

293 4.1. *Applicability of the double-subduction models to the Neo-Tethyan systems*

294 Based on the available field, petrological, paleo-magnetic and geochemical information,
295 we consider the following Neo-Tethyan subduction systems: i) Trans-Tethyan intra-oceanic
296 system, ii) India-Andaman-Burma subduction system, and iii) Amirante-India-Eurasia to discuss
297 their evolution in the light of the present SDDS models. These subduction systems are chosen as
298 their tectonic settings have been well-constrained by combining geological and geophysical
299 observations in recent studies. Additionally, seismic observations indicate that the subducted slabs
300 in these systems rested in the upper parts of the lower mantle (Van Der Voo et al., 1999; Yang et
301 al., 2022). To implement this slab configuration in the simulations, our modelling excludes the
302 phase changes at the 660-km transition.

303 4.1.1. *Cretaceous evolution of the Trans-Tethyan System*

304 The Trans-Tethyan intra-oceanic system (Fig. 7a) evolved through multiple subduction
305 episodes in the Neo-Tethys during the Cretaceous to Early Tertiary period as discussed earlier in
306 Section 1. The convergence history, derived from the plate reconstructions and paleomagnetic
307 interpretations (Cande and Stegman, 2011; Copley et al., 2010; Van Hinsbergen et al., 2011) reveal
308 that, during the Indo-Eurasian convergence the Indian Plate had a rapid northward drift moving at
309 extremely high velocities >12 cm/year from 60 Ma to 50 Ma (Copley et al., 2010; Molnar & Stock,
310 2009), which subsequently reduced to 8 cm/year at ~ 40 Ma that marks the timing of India-Eurasia
311 collision (Maiti et al., 2021). The oceanic plate model presented in Section 3.1 provides new
312 insights into the geodynamic evolution of the Trans-Tethyan intra-oceanic system. The subducting
313 oceanic plates in the model, RSZ and FSZ represent the frontal oceanic part of the Indian Plate

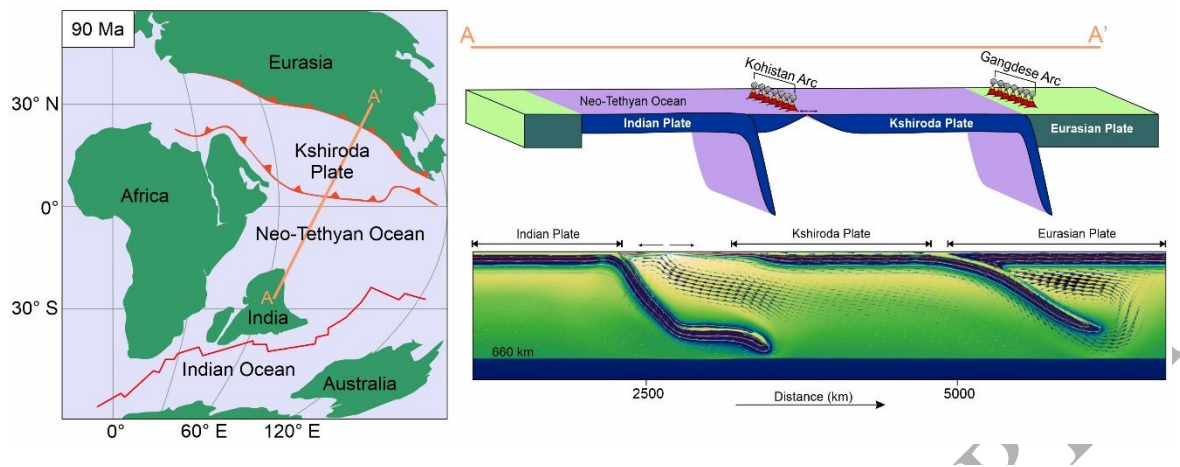


Figure 7: a) Sketch showing the reconstructions of Neo-Tethyan plate boundaries at ~ 90 Ma modified after Jagoutz et al., 2015 b) Cross section along AA' showing slab geometries and distances between the two prominent subduction systems giving rise to the double subduction process. c) Time snapshot (16 Myr) of the oceanic SDDS model which simulates the Cretaceous evolution of the Trans-Tethyan System.

314 and the Kshiroda Plate, respectively, in association with the Eurasian overriding plate (Fig 7a,b).
 315 Pre-existing lithosphere-scale weaknesses, such as transform faults or oceanic fracture zones
 316 between the Kshiroda and the Indian Plate nucleated the subduction initiation at the leading edge
 317 of the Indian oceanic lithosphere, almost synchronously accompanied by opening of a proto back-
 318 arc extensional zone. The subduction event resulted in arc formation, preserved as the Kohistan-
 319 Ladakh Arc in the Himalaya-Tibet Mountain system (Bouilhol et al., 2013). A correlation of the
 320 arc initiation timing with the paleomagnetic data reveal that the Kohistan-Ladakh Arc rocks and
 321 ophiolites in the Tsangpo-suture zone formed nearly at the equator position (Aitchison et al., 2000).
 322 After $\sim 4-5$ Myr from the intra-oceanic subduction initiation, the passive margin between the
 323 Kshiroda and Eurasian Plates became active to form a second subduction (FSZ) (Fig. 7c), which
 324 gave rise to the Gangdese-Karakoram continental arc. The paleomagnetic data of magmatic rocks
 325 indicate that the arc formed at a latitudinal position $\sim 20^\circ-25^\circ$ N, ~ 2500 km from the Kohistan Arc
 326 present location, which is consistent with the present model estimates. The model convergence
 327 history reveals a period of rapid convergence with velocities $> \sim 15$ cm/year for a period of ~ 8 Myr

1
2
3
4
5
6
7
8
9
10
11
12
13
14
15
16
17
18
19
20
21
22
23
24
25
26
27
28
29
30
31
32
33
34
35
36
37
38
39
40
41
42
43
44
45
46
47
48
49
50
51
52
53
54
55
56
57
58
59
60
61
62
63
64
65

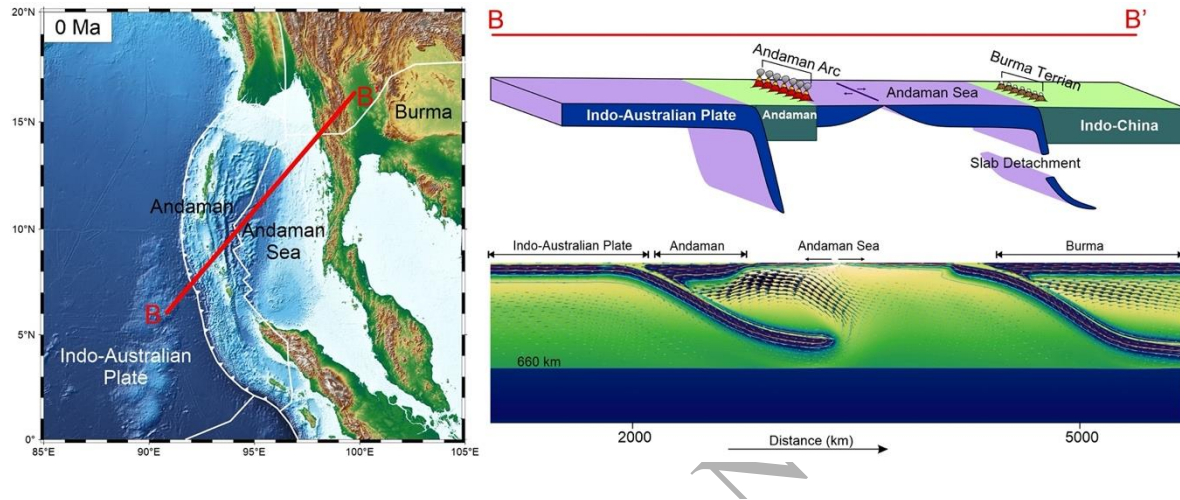
before reducing to ~ 9 cm/year in the later phase of the model run. This two-stage kinematic evolution is also in agreement with the Cretaceous convergence history of the Indo-Eurasian system prior to the Early Cenozoic slowdown (Molnar and Stock, 2009).

The existence of an extensional zone, namely the Kohistan Arc between two active subduction zones decoupled the oceanic plate, which in turn freed the rear slab from slab pull of the frontal subduction zone. According to this model, high convergence rates can originate in double subduction systems, even in the absence of any slab pull-force transfer from the frontal to the rear subduction zone. However, our model estimates yield the absolute Indian plate velocity (PM1: $\sim 11-6$ cm/year) lower than those interpreted from paleomagnetic records. This discrepancy probably results from additional influences of other geodynamic processes, e.g., push force from the Reunion plume to the Indian Plate (Pusok and Stegman, 2020), which are excluded in the modelling. This poses a limitation in the present analysis. Addition of these factors might lead to convergence velocities significantly higher than present model values. However, such positive influences were perhaps countered by the presence of Indian continent, which would act as a sort of keel to reduce the plate velocity. Further model analyses are required to pinpoint their additional effects.

4.1.2. Cenozoic evolution of the Andaman System

In the case of the Andaman Subduction System (Fig. 8a, b), the active subduction occurs currently at the northern flank of the Java trench where the oceanic part of the Indian Plate subducts at a low angle to the arc-trend beneath a small overriding-continental block (Fig. 5). This continental fragment, which is a detached part of the larger Indian Plate occurs parallel to the volcanic arc, forming the Andaman Island Chain. The Pliocene-Holocene volcanism in the inner arc of the Java Trench suggests that the subduction has remained active since the late Miocene

1
2
3
4 351 (Acharyya et al., 1991; Sengupta et al., 1990). The Andaman Sea, a manifestation of extensional
5
6 352 tectonics and other similar basins in this region also opened up in the late Miocene (Curry, 2005).
7
8
9 353 The Andaman Ophiolites occur in a flat-lying arrangement, showing a close spatial association
10
11 354 with a zone of negative gravity anomalies that suggest their occurrence as thin sub-horizontal



12
13
14
15
16
17
18
19
20
21
22
23
24
25
26
27
28
29
30 Figure 8: a) Bathymetric map of the Andaman Subduction Zone b) 3D block diagram of important
31 components in the present-day Andaman–Nicobar subduction system along the BB' profile showing
32 slab geometries and spatial relation between the two subduction systems and the Andaman micro-
33 continent. c) Time snapshot (15 Myr) of the oceanic-continent double subduction model which
34 simulates the last 30 Myr evolution of this eastern Neo-Tethyan region.

35
36 355 bodies. Moreover, the ophiolite suits range in age between late Mesozoic and early Eocene, much
37
38 356 older than the Andaman Sea crust. These observations indicate that the Andaman and other related
39
40
41 357 ophiolites farther north in this convergent zone were derived from a suture to the east during late
42
43 358 Oligocene time and emplaced as nappes during the middle Eocene. The geochronological order
44
45 359 indicates the existence of a second subduction zone at the time of late-Miocene subduction
46
47
48 360 (continuing to present day) and opening of the Andaman Sea (Khan & Chakraborty, 2005). Our
49
50 361 micro-continent-oceanic plate model (Fig. 4) explains how the SDDS dynamics controlled such a
51
52 362 tectonic evolution in the Andaman convergent belt. The FSZ simulates the mid-Eocene subduction
53
54 363 event where the Indo-Australian oceanic lithosphere continued to subduct beneath the Burma Plate
55
56
57 364 (equivalent to the stiffer OP in the model). The model setup produces an extensional spreading
58
59
60
61
62
63
64
65

1
2
3
4 365 centre as a consequence of some pre-existing lithospheric flaws, switching a remarkable change
5
6
7 366 in the evolutionary course of the single-subduction system. The mechanical weakness might have
8
9 367 developed due to the southward propagation of dextral motion in the Sagaing Fault System, which
10
11 368 was active well before Miocene to set the mechanical conditions necessary for the Andaman Sea
12
13
14 369 opening. The formation of this extensional zone eventually led to the late Miocene emergence of
15
16 370 the Andaman Sea basin. The microcontinental fragment (*cf.* Andaman continental block)
17
18
19 371 eventually decoupled itself from the ongoing subducting slab, and initiated a second subduction in
20
21 372 the same region, as observed in our model at ~6 Myr (Fig. 8c). The newly formed subduction can
22
23
24 373 be compared with the presently active Indo-Australian oceanic subduction below the Java Trench.
25
26 374 The model suggests that both the subduction remained active for a considerable time (~24 Myr)
27
28
29 375 and facilitated the Indo-Australian Plate motion relative to the Burma Plate. With time, the younger
30
31 376 oceanic lithosphere formed at the Andaman Sea spreading centre drifted to the trench close to the
32
33 377 Burma Plate and resulted in oceanic slab detachment as the lithosphere failed to gain density
34
35
36 378 required for the mid-Eocene subduction.

379 *4.1.3. Post-Cretaceous Indo-Eurasian Convergence*

40
41 380 The India-Eurasia convergence during the Cenozoic period had a collision between continental
42
43 381 India and the Kohistan arc (Burg, 2011) and subsequently, with the Gangdese-Karakoram
44
45
46 382 continental arc, resulting in the closure of the Neo-Tethyan basin. The opening of the Carlsberg
47
48
49 383 Ridge in the Indian Ocean basin characterises the region south of the Indian continent (Fig 9c).
50
51 384 The multiple continental plate model demonstrates the Cenozoic Indo-Eurasian collisional tectonic
52
53 385 history very well. This model reproduces the collision of the Indian continental plate with the
54
55
56 386 Eurasian Plate (~45 Ma) (Ding et al., 2005, 2016; Khan et al., 2009) when the oceanic subduction
57
58 387 below Eurasia was active. Interestingly, the Carlsberg ridge had a fast spreading in late Cretaceous
59
60
61
62
63
64
65

388 (Merkouriev and Sotchevanova, 2003), which is found in our model that forms a spreading ridge
 389 and a second subduction in the ridge's vicinity. Based on our model results, we propose that the
 390 subduction occurred at the present-day position of the Amirante Trench- a trough-like feature,

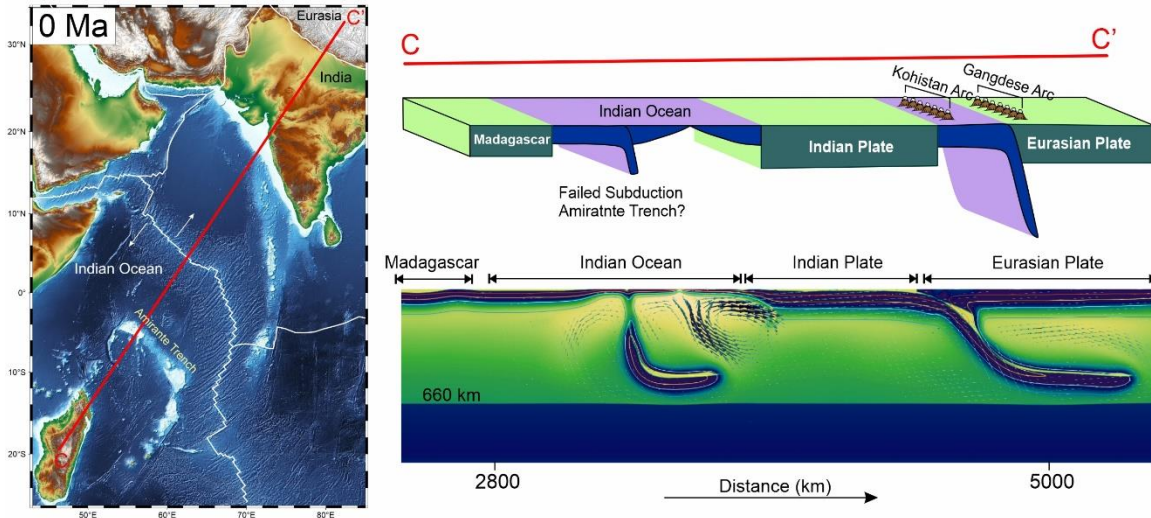


Figure 9: a) Bathymetric map of the Indo-Eurasian convergence zone and its related features b) Cross section along CC' showing slab geometries and distances between the prominent subduction features resulting in the convergence of the Indian plate with the Eurasian plate c) Time snapshot at 20 Myr of the multiple continent SDDS model which simulates the Post-Cretaceous evolution of the Indo-Eurasian collision zone.

391 approximately 600 km long in the western Indian Ocean (Fig. 9a). Geological and geophysical
 392 studies show evidence of partial or limited subduction within the trench (Miles, 1982). As observed
 393 in our model, the subduction was active in this region for ~4 Myr but ceased its activity following
 394 the slab detachment under the influence of a continental block (analogous to the Madagascar
 395 continental fragment in nature). The collision between the Indian and Eurasian continents led to a
 396 dramatic shift from retreating to advancing trench motion and a decrease in the Carlsberg ridge
 397 spreading rate, both of which are compatible with the model results. Our model results show that
 398 this tectonic system did not lead to the formation of a matured SDDS zones due to the influence
 399 of the continental blocks.

400 4.2. Double-subduction evolution by feedback mechanisms

1
2
3
4 401 The present model experiments demonstrate that a double-subduction system can grow
5
6 402 spontaneously from pre-existing weak zones (Bercovici and Ricard, 2014; Maunder et al., 2020)
7
8
9 403 under slab-pull dynamics. The two subduction zones in such systems, however, evolve in a
10
11
12 404 competing mode, one suppressing the other, ultimately leading to their unequal development on a
13
14 405 million-year timescale. To illustrate this, consider our double-subduction model for an oceanic
15
16 406 plate setting as applicable to the Trans-Tethyan System evolution during Cretaceous. The model
17
18
19 407 shows synchronous initiation of subduction at two lithospheric weak zones (Rear and Fore
20
21 408 Subduction Zone: RSZ and FSZ), but one of them (RSZ) preferentially becomes the most active
22
23
24 409 zone (subduction velocity: ~11 cm/yr), suppressing the other slab (FSZ) motion to remain
25
26 410 significantly weak (~1.5 cm/yr). This competing double-subduction dynamics causes the second
27
28
29 411 subduction to become more active once the first subducting slab encounters resistance at the lower
30
31 412 mantle at 660 km. The reduced slab motion, coupled with a trench retreat motion in one subduction
32
33
34 413 has a feedback effect on the second subduction in accelerating slab motion (~1.5 to ~6 cm/yr). To
35
36 414 quantitatively evaluate the competing evolution of a double subduction system, we compare the
37
38
39 415 SDDS model results with those from a subduction model, containing a single subduction system
40
41 416 equivalent to the FSZ (details provided in Supplementary S1). The model comparison reveals that
42
43 417 the RSZ activity significantly delays the FSZ initiation (~13.4 Myr), which, in contrast, begins to
44
45
46 418 occur much quicker (3.4 Myr) in the single subduction model (Fig. S2). In addition, the FSZ
47
48 419 activity, in overall becomes significantly sluggish due to its interaction with the RSZ in the oceanic
49
50
51 420 double subduction system.

52
53 421 The other two model settings (Figs. 4,5) show similar feedback effects on the development
54
55
56 422 of double-subduction systems. In the microcontinent-bearing oceanic plate setting, analogous to
57
58 423 that of Andaman subduction system, the double subduction processes operate almost equally (Fig.
59
60
61
62
63
64
65

1
2
3
4 424 4), forming a spreading centre between the two subduction zones. However, the new lithosphere
5
6
7 425 formed in the spreading centre causes the frontal subduction zone (FSZ) to undergo slab
8
9 426 detachment, which in turn facilitates the slab motion in the rear subduction zone (RSZ). The
10
11 427 multiple continental plate setting also shows a time-dependent interaction between the RSZ and
12
13
14 428 FSZ during their evolution. The FSZ slab motion hardly allows the RSZ to become significantly
15
16 429 active until the slab encounters the lower mantle to slow down its motion. The RSZ slab starts to
17
18
19 430 actively sink when the RSZ almost reaches the upper-lower mantle boundary after a time of ~11
20
21 431 Myr. The feedback direction reverses as the RSZ experiences slab detachment due to resistance
22
23
24 432 offered by the continent in the rear subducting oceanic plate. The paleo-trench at Amirante is an
25
26 433 excellent example of subduction that failed to attain maturity due to the influence of the
27
28
29 434 Madagascar continental plate. Thus, the model examples discussed here suggest that the SDDS
30
31 435 systems generally evolve with a feedback relation between the two subduction zones that mutually
32
33 436 interact with one another. To advance these findings, further studies are required to compare the
34
35
36 437 model results with corresponding single-subduction model simulations and quantify the additional
37
38 438 effects of slab-slab interaction in the SDDS systems.

41 439 *4.3. Influence of continental heterogeneities*

42
43 440 Previous studies have shown that the complexity in double-subduction systems, as compared
44
45
46 441 to single-subduction settings, originates mainly from the effects of inter-slab interactions in plate
47
48 442 bending, coupled with additional factors, contrasting plate ages, plate dimensions, rheology, and
49
50
51 443 inter-slab distance (Mishin et al., 2008; Cížková & Bina 2015; Holt et al., 2017). This study
52
53 444 identifies the presence of microcontinental blocks or continental plates in oceanic plate tectonic
54
55
56 445 settings as an additional influential factor in the dynamics and stability of a double-subduction
57
58 446 system. Microcontinents are mostly surrounded by oceanic crust, and they form by extension and
59
60
61
62
63
64
65

1
2
3
4
5
6
7
8
9
10
11
12
13
14
15
16
17
18
19
20
21
22
23
24
25
26
27
28
29
30
31
32
33
34
35
36
37
38
39
40
41
42
43
44
45
46
47
48
49
50
51
52
53
54
55
56
57
58
59
60
61
62
63
64
65

breakup of continental masses, followed by plate boundary relocations. Jan-Mayen in the north-east Atlantic Ocean (Gaina et al., 2009; Peron-Pinvidic et al., 2012), Andaman in the Indian Ocean (Bandyopadhyay et al., 2020) and several small, isolated islands around Australia (Gaina et al., 2003) are typical examples of microcontinents. Our microcontinent-oceanic double-subduction model suggests that such microcontinents play a vital role in localizing a spreading centre (location of new lithosphere generation) between the two subduction zones. The spreading centre, however, remains active for a specific time span, and its activity weakens following the slab detachment in the FSZ. This mechanism can be directly compared to the opening of the Andaman Sea extensional zone, synchronous to the initiation of the present-day subduction below the Andaman microcontinent.

The model results show that an oceanic plate setting in the absence of any continental blocks can readily form a double subduction system, initiated by pre-existing lithospheric weak zones in the plate setting. However, a buoyant continental fragment selectively prevents the subduction zones in front of this plate to mature with time, and forces the system to evolve unequally at the two trenches. Similarly, a multiple-continental assemblage reduces the convergence rates due to their buoyancy and continent-arc collision effects, described as *transference* by Stern (2004) to show the accretion-assisted continental growth mechanism. The reducing convergence rates result in tensile stresses in the subducting slab, eventually leading to slab detachment (Fig. 5). The model results suggest that microcontinental blocks can greatly influence the evolution of subduction processes, as reported from several natural subduction systems, such as the northern Luzon, the Puysegur (New Zealand) and the Andaman subduction zones (Bandyopadhyay et al., 2020; Zhu et al., 2023). The microcontinents provide a potential location of passive continental margin that transforms into a tectonically active region by subduction initiation as evident in the evolution

1
2
3
4 470 Andaman subduction system. Due to their lower mechanical strength, compared to that of large
5
6 471 continental plates they localize subduction and facilitate the process to occur at faster rates.
7
8

9 472 *4.4. Subduction-driven spreading centres: location of new plate generation*
10

11 473 Generally, single-subduction systems involve slab rollback, which is often accommodated
12
13
14 474 by horizontal extension and formation of a spreading centre (back-arc basin) in the overriding
15
16 475 plate. Double-subduction systems in an oceanic plate setting, on the other hand, forces the rear
17
18 476 trench to retreat at fast rates as the frontal plate moves in the opposite direction, offering less
19
20 477 resistance to the rear slab. This kinematic state results in formation of a spreading centre at the rear
21
22 478 trench, which eventually acts as a site for new lithosphere generation. This mechanism allows the
23
24 479 RSZ to accommodate slab roll back without involving overriding plate kinematics, as in a single-
25
26 480 subduction setting. This model study thus brings out the importance of such spontaneous spreading
27
28 481 centre formation in the SDDS evolution within large oceanic plates.
29
30
31
32

33
34 482 Our modelling demonstrates that spreading centres crucially control the subduction
35
36 483 dynamics in transforming a double- to a single-subduction system. The microcontinent-oceanic
37
38 484 plate model shows the development of large tensile stresses in the region between the older
39
40 485 subducting plate and the newly formed lithosphere at the trench, which causes the older slab to
41
42 486 experience detachment. The slab break-off eventually stops the subduction activity, leaving the
43
44 487 other subduction active. Spreading centres also play an important role in the onset of convergent
45
46 488 setting and promotes decoupling in a large oceanic plate (e.g., *oceanic plate model*, Fig. 3). Such
47
48 489 tectonic processes are observed in other natural systems, for example, the Cocos-Nazca spreading
49
50 490 centre where the spreading centre formed by splitting of the oceanic lithosphere, giving rise to the
51
52 491 Farallon plate break up in the early Miocene.
53
54
55
56
57

58 492
59
60
61
62
63
64
65

5. Conclusions

The key results of this research are two-fold: firstly, it unveils the intricate mechanisms governing the development of same-dip double subduction (SDDS) systems. Secondly, it provides new insights into the role of SDDS dynamics in the Neo-Tethyan tectonic evolution. The principal findings of this study are summarized as follows: 1) SDDS are initiated spontaneously in presence of lithospheric-scale mechanical weaknesses, e.g., faults, without any aid of kinematic perturbations, in contrary to that suggested in earlier studies. Throughout the temporal progression of a SDDS system, the two subducting slabs mutually affect their kinematics and subduction-driven flow patterns in the mantle wedges as well as asthenosphere. 2) SDDS systems can remain active for a long period of time (>25 Myr) in an oceanic setting, and eventually attain exceptionally high convergence velocities, 16-17 cm/year during its extended period (~5 Myr) of activity, depending on the slab ages at the trenches. These model findings explain the development of a self-sustaining SDDS responsible for the anomalously Indo-Eurasian high-convergence velocity condition in the Cretaceous Neo-Tethyan evolution. 3) The presence of continental blocks in the initial plate setting greatly influences the SDDS dynamics, forcing the double subduction zones to localize preferentially at their passive margins with the oceanic plates. They grow almost equally, forming a spreading centre between the two trenches on a time scale of 25 Myr. This SDDS model accounts for the Cenozoic tectonic evolution in the eastern Neo-Tethyan region, which ultimately formed the Andaman subduction system. 4) In an initial plate configuration with multiple continental fragments or plates, the latter can cause one of the SDDS slabs to halt its motion, resulting in a double to single-subduction transformation, which occurred in the Amirante-India-Eurasia subduction system during the Cenozoic evolution of Neo-Tethys.

1
2
3
4 **516 Declaration of Competing Interest**

5
6
7 517 The authors declare that they have no known competing financial interests or personal
8
9 518 relationships that could have appeared to influence the work reported in this article.

10
11
12 519
13
14 **520 Acknowledgments**

15
16
17 521 We thank two anonymous reviewers and Editor Carolina Lithgow-Bertelloni for their constructive
18
19 522 suggestions and incisive comments, which have greatly improved our present study. The work has
20
21
22 523 been performed under the Project HPC-EUROPA3 (INFRAIA-2016-1-730897), with the support
23
24 524 of the EC Research Innovation Action under the H2020 Programme; in particular, A.R. gratefully
25
26
27 525 acknowledges the support of Durham University and the computer resources and technical support
28
29 526 provided by EPCC, University of Edinburgh. A.R. gratefully acknowledges CSIR, India for
30
31
32 527 awarding research fellowship grants (09/096(0940)/2018- EMR-I). This work used the ARCHER2
33
34 528 UK National Supercomputing Service (<https://www.archer2.ac.uk>). The DST-SERB is
35
36
37 529 acknowledged for supporting this work through the J.C. Bose fellowship (JBR/2022/000003) to
38
39 530 N.M.

40
41
42 531
43
44 **532 Data Availability Statement**

45
46
47 533 The authors confirm that all the data used to support the findings of this study are available within
48
49 534 the article and as supplementary materials. All aspects of UNDERWORLD 2 (Mansour, J., et al.,
50
51
52 535 2020) can be checked here (<https://doi.org/10.5281/zenodo.6820562>).

53
54 536

Description	Symbol	Unit	Default Values
-------------	--------	------	----------------

55
56
57
58
59
60
61
62
63
64
65

1	Thermal expansion coefficient	α	K^{-1}	3×10^5
2				
3				
4				
5				
6				
7	Thermal diffusivity	κ	$\text{m}^2 \text{s}^{-1}$	10^{-6}
8				
9	Reference density	ρ_0	kg m^{-3}	3300
10				
11	Surface temperature	T_s	K	273
12				
13				
14	Potential temperature	T_m	K	1673
15				
16	Adiabatic temperature gradient	dT/dz	K km^{-1}	0.37
17				
18				
19	Gravitational acceleration	g	m s^{-2}	9.81
20				
21	Maximum viscosity	η_{max}	Pa s	1.0×10^{24}
22				
23	Minimum viscosity	η_{min}	Pa s	1.0×10^{19}
24				
25				
26	Crust viscosity	η_c	Pa s	1.0×10^{20}
27				
28				
29				
30				
31	Dislocation creep (Upper Mantle)			
32				
33	Activation energy	E	kJ mol^{-1}	540
34				
35	Activation volume	V	$\text{cm}^3 \text{mol}^{-1}$	10
36				
37				
38	Pre-factor	A	$\text{Pa}^n \text{s}^{-1}$	4.1×10^{15}
39				
40	Exponent	n	-	3.5
41				
42				
43				
44				
45	Diffusion creep (Upper and Lower mantle)			
46				
47	Activation energy	E	kJ mol^{-1}	300 (UM & LM)
48				
49	Activation volume	V	$\text{cm}^3 \text{mol}^{-1}$	4.5 (UM), 1.58 (LM)
50				
51				
52	Pre-factor	A	$\text{Pa}^1 \text{s}^{-1}$	1.87×10^9 (UM)
53				
54				
55				1.77×10^{14} (LM)
56				
57	Exponent	n	-	1
58				
59				
60				
61				
62				
63				
64				
65				

Plastic yielding			
Cohesion	C_0	MPa	20
Friction coefficient	μ	-	0.1
Maximum yield stress	τ_{max}	MPa	500

Table 1: List of model parameters and their corresponding values chosen for the numerical simulations.

6. Appendix A

6.1 Governing equations

We build numerical, time-evolving, dynamically consistent thermomechanical subduction models in 2-D Cartesian domains within a theoretical framework of computational fluid dynamics (CFD), implemented by using the UNDERWORLD2 code (Mansour et al., 2020). This CFD simulation study assumes an incompressible Boussinesq fluid flow, approximated to the long-time (multi-million year) scale kinematic state of Earth's mantle. This approximation accounts for only buoyancy (body force term), treating all other effects of density fluctuations negligibly small in the momentum equation. We use the continuity and momentum conservation equations in our modelling to describe spontaneous flows in our model driven by density anomalies. The expressions of these equations are, respectively,

$$\frac{\delta u_i}{\delta x_i} = 0 \quad (1)$$

$$-\frac{\delta P}{\delta x_i} + \frac{\delta \sigma_{ij}}{\delta x_j} + \rho g_i = 0 \quad (2)$$

1
2
3
4 550 where v_i is the velocity vector. In Eq. (2) the inertial forces are neglected, as applicable to long
5
6
7 551 term flows in the mantle. σ_{ij} can be decomposed into the isotropic (σ^o_{ij}) and the deviatoric stress
8
9 552 (τ_{ij}) tensors as,

$$\sigma_{ij} = \sigma^o_{ij} + \tau_{ij} \quad (3)$$

11
12
13
14
15
16 553 such that

$$\sigma^o_{ij} = P\delta_{ij} \quad (4)$$

$$\tau_{ij} = 2\eta\dot{\epsilon}_{ij} = \eta\left(\frac{\partial u_i}{\partial x_j} + \frac{\partial u_j}{\partial x_i}\right) \quad (5)$$

17
18
19
20
21
22
23
24
25
26 554 where $\dot{\epsilon}_{ij}$ is the strain rate tensor. Substituting Eq. (4) & (5) into Eq. (2) gives rise to the Stokes
27
28
29 555 equation with pressure and velocity as two unknown variable parameters. Applying the model
30
31 556 boundary conditions, we numerically solve the continuity and Stokes equations in a pre-defined
32
33
34 557 2D Cartesian domain to derive the velocity and pressure in the model domain.

35
36 558 The thermal evolution of a subduction system is dictated by combined effects of advective heat
37
38
39 559 transfer, thermal diffusion, and heat sources/sinks within the system, which we tackle with the
40
41 560 following heat equation.

$$\rho C_p \frac{DT}{Dt} = \frac{\partial q_i}{\partial x_i} + \rho Q, \quad (6)$$

42
43
44
45
46
47
48 561 where Q is the rate of internal heat production per unit volume, T is the temperature, ρ is the
49
50 562 material density and C_p is the specific heat. q represents the rate of diffusional heat transfer,
51
52
53 563 described by Fourier's law as,

$$q_i = -k \frac{\partial T'}{\partial x_i}, \quad (7)$$

1
2
3
4 564 where k is the thermal conductivity and T' is the nonadiabatic temperature. Substituting Eq. (7)
5
6
7 565 into (6) and expanding considering the definition of material derivative, gives

$$\frac{\partial T}{\partial t} + u_i \cdot \frac{\partial T'}{\partial x_i} = \kappa \nabla^2 T' + \frac{Q}{C_p} \quad (8)$$

10
11
12
13
14 566 where $\kappa = \frac{k}{\rho C_p}$, which represents the thermal diffusivity. T' is replaced by the adiabatic
15
16
17
18 567 temperature (T_a) of the system as a function of depth (z) obtained from the relation:

$$T_a = T' + z \left(\frac{\partial T'}{\partial z} \right) = T' + z \left(\frac{\alpha g T_p}{C_p} \right), \quad (9)$$

19
20
21
22
23
24
25 568 where T_p is the mantle potential temperature and α is the coefficient of thermal expansion, which
26
27
28 569 was set at a value of $3 \times 10^{-5} \text{ K}^{-1}$. Considering $C_p = 1260 \text{ J/kg/K}$ for Earth's mantle, a resultant
29
30
31 570 adiabatic temperature gradient of 0.4 K/km is added to the nonadiabatic temperature of the mantle.
32
33 571 The energy conservation equation (8) is solved using the Semi-Lagrangian Crank-Nicholson
34
35 572 (SLCN) method (Spiegelman and Katz, 2006), built upon the potencies of the Crank-Nicolson
36
37
38 573 scheme for diffusion and the semi-Lagrangian scheme for advection. The SLCN method has been
39
40 574 found to be unconditionally stable, allowing large time-step sizes. We impose constant (Dirichlet)
41
42
43 575 and zero-flux (Neumann) on the top and bottom boundaries, respectively to solve the energy
44
45 576 equation. The model surface temperature is set initially at 0°C , whereas the initial model basal
46
47
48 577 temperature at 1800°C .

49
50 578 We use half-space cooling profiles to constrain the thermal structures of model lithospheric
51
52 579 plates corresponding to their assigned ages, considering a thermal diffusivity value of $10^{-6} \text{ m}^2/\text{s}$
53
54
55 580 (van Hunen and Allen, 2011), and a mantle potential temperature of 1400°C (Holt and Condit,
56
57 581 2021). The model density parameters are chosen as a function of the assigned temperatures, taking
58
59
60
61
62
63
64
65

1
2
3
4 582 into account the thermal properties and their evolution following the momentum equation. For
5
6
7 583 temperature dependent density variations, we adopt the equation of state,

$$\rho = \rho_r(1 - \alpha(T - T_p)) \quad (10)$$

10
11
12
13 584 where ρ_r denotes the reference mantle density at the mantle potential temperature, which is set at
14
15 585 3300 kg/m^3 .

18 586 6.2. Rheological considerations

20
21 587 We model the mantle rheology in the framework of a composite creep law that combines
22
23 588 diffusion creep (η_{diff}), dislocation creep (η_{disl}), and plastic yielding (η_{yield}). An Arrhenius
24
25
26 589 temperature and pressure dependence of the activation volume (V) and the activation energy (E)
27
28 590 (Hirth and Kohlstedt, 2004) is chosen to describe the creep laws for mantle silicates, which leads
29
30
31 591 to the diffusion/dislocation-controlled viscosity,

$$\eta_{diff/disl} = A \frac{-1}{n} \dot{\epsilon}^{\frac{1-n}{n}} \exp\left(\frac{E + P_1 V}{nRT_a}\right) \quad (11)$$

32
33
34
35
36
37
38 592 where A is a pre-factor, n is the stress exponent ($n = 1$ and 3.5 for diffusional and dislocation creep,
39
40 593 respectively), R is the gas constant and P_1 is the lithostatic pressure. It is usually observed that
41
42
43 594 lithostatic pressure enhances the yield strength of mantle material by different stress-limiting
44
45 595 mechanisms. In contrast, material strength can be reduced as a consequence of brittle yielding
46
47
48 596 (Kohlstedt et al., 1995) near the surface. These two yield mechanisms are combined into a
49
50
51 597 simplified plastic rheology (van Hunen and Allen, 2011), and the viscosity is described as,

$$\eta_{yield} = \frac{\tau_{yield}}{2\dot{\epsilon}} \quad (12)$$

52
53
54
55
56
57 598 and τ_{yield} denotes the yield strength, expressed by the following relation.
58
59
60
61
62
63
64
65

$$\tau_{yield} = \min (C + \mu P, \tau_{max}) \quad (13)$$

599 where C (= 20 MPa) is the initial cohesion, μ (= 0.1) is the friction coefficient, and τ_{max} is the cut-
 600 off yield stress value. The harmonic mean of the three types of viscosity is considered to determine
 601 an effective model viscosity (η_{eff}),

$$\frac{1}{\eta_{eff}} = \frac{1}{\eta_{diff}} + \frac{1}{\eta_{disl}} + \frac{1}{\eta_{yield}} \quad (14)$$

602 The activation volumes (V) and energies (E) values (Table 1) chosen in our modelling are
 603 consistent with the experimental estimates for dry olivine (Karato and Wu, 1993). We have
 604 considered the value of pre- factor A for the upper mantle based on the following findings, 1) an
 605 effective viscosity in the order of 10^{20} Pa in the shallow part of upper mantle (Hager, 1990), and
 606 2) seismic anisotropy implying dominantly dislocation creep in the majority part of mantle
 607 (Becker, 2006). Diffusional creep is recognized as the principal mechanism to determine the lower-
 608 mantle rheology (Karato & Wu, 1993). A range of estimates suggest its viscosity significantly
 609 higher than the upper-mantle viscosity. The calculated creep pre-factor yields a value of 3×10^{22}
 610 at the 660 km transition (Čížková et al., 2012), which increases continuously with depth (Fig. 2).

611 The top crustal layer in our model is assigned a constant viscosity of 1×10^{20} Pa s. We use
 612 Eq. (12) to simulate brittle failure in this layer, assuming a low value (10 MPa) of its cohesion.
 613 This rheological consideration aims to reproduce the mode crust with yield strength lower than
 614 that of the lithosphere. This modelling manipulation allows us to introduce decoupling of the
 615 subducting slab from the overriding plate and facilitate the plate convergence process. The mantle
 616 lithosphere strength is determined from the upper viscosity cut-off values (1×10^{24} Pa s), except
 617 for regions where we preferentially activate plastic yielding. For the overriding plate (OP), the
 618 upper limit of viscosity is increased to 2.5×10^{24} Pa s to obtain a slightly higher stiffness. We

1
2
3
4 619 model the crust and the lithosphere individually single layers without any internal rheological
5
6 620 stratification. Considering the long-term process of our present concern, the effects of elastic
7
8
9 621 deformation are completely excluded. We add passive tracers in the compositional field within the
10
11
12 622 regions of interest to track the plate motion and deformation during the model run.

14 623 *6.3. Model Setup*

16
17 624 We meshed the 2D domain by smaller quadrilateral elements with a mesh resolution of 512
18
19 625 elements in the vertical direction, which provides an element width of ~ 2 km, and a particle density
20
21
22 626 of 50 tracers per element. These Lagrangian tracer particles used to track advecting materials and
23
24 627 their corresponding physical properties are mapped to quadrature points with nearest-neighbour
25
26
27 628 interpolation (Sandiford and Moresi, 2019). All models were subjected to $g = 9.8 \text{ m/s}^2$, where g is
28
29 629 the acceleration due to gravity. The model has free-slip ($v_y = 0$) conditions assigned to the bottom
30
31
32 630 and top boundaries, whereas periodic boundary condition is imposed on the sidewalls.

34 631 For the temperature boundary condition, we impose constant (Dirichlet) and zero-flux
35
36
37 632 (Neumann) on the top and bottom boundaries, respectively to solve the energy equation. We use
38
39 633 half-space cooling profiles to constrain the thermal structures of model lithospheric plates
40
41
42 634 corresponding to their assigned ages, considering a thermal diffusivity value of $10^{-6} \text{ m}^2/\text{s}$ (van
43
44 635 Hunen & Allen, 2011), and a mantle potential temperature of 1400° C (Holt & Condit, 2021). The
45
46
47 636 model density parameters are chosen as a function of the assigned temperatures, taking into
48
49 637 account the thermal properties and their evolution following the momentum equation.

51 638 *6.4. Numerical Scaling, Mesh Refinement Tests and Model validation*

54 639 The governing equations (Section 6.1) and physical parameters are non-dimensionalized to
55
56
57 640 implement them for the model simulations utilizing the UNDERWORLD2 scaling module. The
58
59 641 model results, corresponding to the reference values of model parameters, are then scaled to their
60
61
62
63
64
65

1
2
3
4 642 equivalent real physical units. The scaling coefficients derived from the base units of length (Kl),
5
6
7 643 mass (Km), time (Kt) and temperature (KT) are set as, $Kl = 1$, $Km = \rho_{ref} \times Kl^3$, $Kt = 1 / (\frac{\eta_{ref} \times Kl}{Km})$
8
9
10 644 and $KT = T_p$, where ρ_{ref} and η_{ref} are the reference density and viscosity, respectively. The scaling
11
12 645 strategy has been implemented to keep buoyancy force as the sole driving factor in subduction of
13
14
15 646 an oceanic lithosphere, assigned a non-dimensional value of 1 to aid the solver efficiency.

16
17 647 We kept a mesh resolution of 1150×512 elements in our modelling. A set of resolution tests
18
19
20 648 was performed for low (576×256 , 288×128 elements) as well as for a much higher resolution
21
22 649 (2300×1024 elements), with an objective to optimize the refined resolution appropriate for
23
24
25 650 subduction initiation modelling and tracking the evolutionary stages of a double subduction system
26
27 651 with thin, weak viscoplastic subduction interfaces, and a composite rheology of the upper mantle.
28
29
30 652 The mesh resolutions and their effects on the trench and subducting plate (SP) velocities are
31
32 653 detailed in the Supplementary Section S4.

33
34 654

35
36 655

37
38 656

39
40 657

41
42 658

43
44 659

45
46 660

47
48 661

49
50 662

51
52 663

53
54 664

55
56
57
58
59
60
61
62
63
64
65

665 **References:**

- 666 Acharyya, S.K., Ray, K.K., Sengupta, S., 1991. The Naga Hills and Andaman ophiolite belt, their
667 setting, nature and collisional emplacement history. *Physics and Chemistry of the Earth* 18,
668 293–315. [https://doi.org/10.1016/0079-1946\(91\)90006-2](https://doi.org/10.1016/0079-1946(91)90006-2)
- 669 Advokaat, E.L., Bongers, M.L.M., Rudyawan, A., BouDagher-Fadel, M.K., Langereis, C.G., van
670 Hinsbergen, D.J.J., 2018. Early Cretaceous origin of the Woyla Arc (Sumatra, Indonesia) on
671 the Australian plate. *Earth Planet Sci Lett* 498, 348–361.
672 <https://doi.org/10.1016/J.EPSL.2018.07.001>
- 673 Aitchison, J.C., Badengzhu, Davis, A.M., Liu, J., Luo, H., Malpas, J.G., McDermid, I.R.C., Wu,
674 H., Ziabrev, S. V., Zhou, M. fu, 2000. Remnants of a Cretaceous intra-oceanic subduction
675 system within the Yarlung–Zangbo suture (southern Tibet). *Earth Planet Sci Lett* 183, 231–
676 244. [https://doi.org/10.1016/S0012-821X\(00\)00287-9](https://doi.org/10.1016/S0012-821X(00)00287-9)
- 677 Arcay, D., Lallemand, S., Abecassis, S., Garel, F., 2020. Can subduction initiation at a transform
678 fault be spontaneous? *Solid Earth* 11, 37–62. <https://doi.org/10.5194/SE-11-37-2020>
- 679 Auzemery, A., Willingshofer, E., Yamato, P., Duretz, T., Sokoutis, D., 2020. Strain localization
680 mechanisms for subduction initiation at passive margins. *Glob Planet Change* 195, 103323.
681 <https://doi.org/10.1016/J.GLOPLACHA.2020.103323>
- 682 Bandyopadhyay, D., van Hinsbergen, D.J.J., Plunder, A., Bandyopadhyay, P.C., Advokaat, E.,
683 Chattopadhyaya, S., Morishita, T., Ghosh, B., 2020. Andaman Ophiolite: An Overview 1–17.
684 https://doi.org/10.1007/978-3-030-39843-9_1
- 685 Becker, T.W., 2006. On the effect of temperature and strain-rate dependent viscosity on global
686 mantle flow, net rotation, and plate-driving forces. *Geophys J Int* 167, 943–957.
687 https://doi.org/10.1111/J.1365-246X.2006.03172.X/2/M_167-2-943-EQ018.JPEG
- 688 Bercovici, D., Ricard, Y., 2014. Plate tectonics, damage and inheritance. *Nature* 2014 508:7497
689 508, 513–516. <https://doi.org/10.1038/nature13072>
- 690 Bouilhol, P., Jagoutz, O., Hanchar, J.M., Dudas, F.O., 2013. Dating the India–Eurasia collision
691 through arc magmatic records. *Earth Planet Sci Lett* 366, 163–175.
692 <https://doi.org/10.1016/J.EPSL.2013.01.023>
- 693 Burg, J.P., 2011. The asia-kohistan-india collision: Review and discussion. *Frontiers in Earth
694 Sciences* 4, 279–309. https://doi.org/10.1007/978-3-540-88558-0_10/COVER
- 695 Cande, S.C., Stegman, D.R., 2011. Indian and African plate motions driven by the push force of
696 the Réunion plume head. *Nature* 2011 475:7354 475, 47–52.
697 <https://doi.org/10.1038/nature10174>
- 698 Čížková, H., Bina, C.R., 2015. Geodynamics of trench advance: Insights from a Philippine-Sea-
699 style geometry. *Earth Planet Sci Lett* 430, 408–415.
700 <https://doi.org/10.1016/J.EPSL.2015.07.004>
- 701 Čížková, H., van den Berg, A.P., Spakman, W., Matyska, C., 2012. The viscosity of Earth’s lower
702 mantle inferred from sinking speed of subducted lithosphere. *Physics of the Earth and
703 Planetary Interiors* 200–201, 56–62. <https://doi.org/10.1016/J.PEPI.2012.02.010>
- 704 Copley, A., Avouac, J.P., Royer, J.Y., 2010. India-Asia collision and the Cenozoic slowdown of
705 the Indian plate: Implications for the forces driving plate motions. *J Geophys Res Solid
706 Earth* 115, 3410. <https://doi.org/10.1029/2009JB006634>
- 707 Corbi, F., Herrendörfer, R., Funicello, F., van Dinther, Y., 2017. Controls of seismogenic zone
708 width and subduction velocity on interplate seismicity: Insights from analog and numerical
709 models. *Geophys Res Lett* 44, 6082–6091. <https://doi.org/10.1002/2016GL072415>

1
2
3
4
5
6
7
8
9
10
11
12
13
14
15
16
17
18
19
20
21
22
23
24
25
26
27
28
29
30
31
32
33
34
35
36
37
38
39
40
41
42
43
44
45
46
47
48
49
50
51
52
53
54
55
56
57
58
59
60
61
62
63
64
65

- Curry, J.R., 2005. Tectonics and history of the Andaman Sea region. *J Asian Earth Sci* 25, 187–232. <https://doi.org/10.1016/J.JSEAES.2004.09.001>
- Dasgupta, R., Mandal, N., 2018. Surface topography of the overriding plates in bi-vergent subduction systems: A mechanical model. *Tectonophysics* 746, 280–295. <https://doi.org/10.1016/J.TECTO.2017.08.008>
- Ding, L., Kapp, P., Wan, X., 2005. Paleocene–Eocene record of ophiolite obduction and initial India-Asia collision, south central Tibet. *Tectonics* 24, 1–18. <https://doi.org/10.1029/2004TC001729>
- Ding, L., Qasim, M., Jadoon, I.A.K., Khan, M.A., Xu, Q., Cai, F., Wang, H., Baral, U., Yue, Y., 2016. The India–Asia collision in north Pakistan: Insight from the U–Pb detrital zircon provenance of Cenozoic foreland basin. *Earth Planet Sci Lett* 455, 49–61. <https://doi.org/10.1016/J.EPSL.2016.09.003>
- Eyuboglu, Y., Dudas, F.O., Zhu, D.C., Liu, Z., Chatterjee, N., 2019. Late Cretaceous I- and A-type magmas in eastern Turkey: Magmatic response to double-sided subduction of Paleozoic and Neo-Tethyan lithospheres. *Lithos* 326–327, 39–70. <https://doi.org/10.1016/J.LITHOS.2018.12.017>
- Faccenna, C., Holt, A.F., Becker, T.W., Lallemand, S., Royden, L.H., 2018. Dynamics of the Ryukyu/Izu-Bonin-Marianas double subduction system. *Tectonophysics* 746, 229–238. <https://doi.org/10.1016/J.TECTO.2017.08.011>
- Gaina, C., Gernigon, L., Ball, P., 2009. Palaeocene-Recent plate boundaries in the NE Atlantic and the formation of the Jan Mayen microcontinent. *J Geol Soc London* 166, 601–616. <https://doi.org/10.1144/0016-76492008-112/ASSET/666CE50E-4E50-4EA4-825A-5FD0D19C5F10/ASSETS/GRAPHIC/601FIG10.JPEG>
- Gaina, C., Müller, R.D., Brown, B., Ishihara, T., 2003. Microcontinent formation around Australia. *Special Paper of the Geological Society of America* 372, 405–416. <https://doi.org/10.1130/0-8137-2372-8.405>
- Ghosh, B., Bandyopadhyay, D., Morishita, T., 2017. Andaman-Nicobar Ophiolites, India: Origin, evolution and emplacement. *Geological Society Memoir* 47, 95–110. <https://doi.org/10.1144/M47.7/ASSET/B51D4277-1DC1-4B58-A0F0-AA65A51742BC/ASSETS/IMAGES/LARGE/M47-1018F08.JPG>
- Gürer, D., van Hinsbergen, D.J.J., Matenco, L., Corfu, F., Cascella, A., 2016. Kinematics of a former oceanic plate of the Neotethys revealed by deformation in the Ulukışla basin (Turkey). *Tectonics* 35, 2385–2416. <https://doi.org/10.1002/2016TC004206>
- Hager, B.H., 1990. Mantle viscosity: a comparison of models from postglacial rebound and from the geoid, plate driving forces, and advected heat flux. *Glacial isostasy, sea-level and mantle rheology* 493–513. https://doi.org/10.1007/978-94-011-3374-6_23/COVER
- Hall, R., 2012. Late Jurassic–Cenozoic reconstructions of the Indonesian region and the Indian Ocean. *Tectonophysics* 570–571, 1–41. <https://doi.org/10.1016/J.TECTO.2012.04.021>
- Hall, R., Spakman, W., 2002. Subducted slabs beneath the eastern Indonesia–Tonga region: insights from tomography. *Earth Planet Sci Lett* 201, 321–336. [https://doi.org/10.1016/S0012-821X\(02\)00705-7](https://doi.org/10.1016/S0012-821X(02)00705-7)
- Heidbach, O., Reinecker, J., Tingay, M., Müller, B., Sperner, B., Fuchs, K., Wenzel, F., 2007. Plate boundary forces are not enough: Second- and third-order stress patterns highlighted in the World Stress Map database. *Tectonics* 26. <https://doi.org/10.1029/2007TC002133>

- 1
2
3
4 754 Hirth, G., Kohlstedt, D., 2004. Rheology of the Upper Mantle and the Mantle Wedge: A View
5 755 from the Experimentalists. *Geophysical Monograph Series* 138, 83–105.
6 756 <https://doi.org/10.1029/138GM06>
7 757 Holt, A.F., Condit, C.B., 2021. Slab Temperature Evolution Over the Lifetime of a Subduction
8 758 Zone. *Geochemistry, Geophysics, Geosystems* 22, e2020GC009476.
9 759 <https://doi.org/10.1029/2020GC009476>
10 760 Holt, A.F., Royden, L.H., Becker, T.W., 2017. The dynamics of double slab subduction. *Geophys*
11 761 *J Int* 209, 250–265. <https://doi.org/10.1093/GJI/GGW496>
12 762 Jagoutz, O., Royden, L., Holt, A.F., Becker, T.W., 2015. Anomalously fast convergence of India
13 763 and Eurasia caused by double subduction. *Nature Geoscience* 2014 8:6 8, 475–478.
14 764 <https://doi.org/10.1038/ngeo2418>
15 765 Jolivet, L., Faccenna, C., Becker, T., Tesauro, M., Sternai, P., Bouilhol, P., 2018. Mantle Flow
16 766 and Deforming Continents: From India-Asia Convergence to Pacific Subduction. *Tectonics*
17 767 37, 2887–2914. <https://doi.org/10.1029/2018TC005036>
18 768 Karato, S.I., Wu, P., 1993. Rheology of the Upper Mantle: A Synthesis. *Science* (1979) 260, 771–
19 769 778. <https://doi.org/10.1126/SCIENCE.260.5109.771>
20 770 Khan, P.K., Chakraborty, P.P., 2005. Two-phase opening of Andaman Sea: a new seismotectonic
21 771 insight. *Earth Planet Sci Lett* 229, 259–271. <https://doi.org/10.1016/J.EPSL.2004.11.010>
22 772 Király, Á., Funicello, F., Capitanio, F.A., Faccenna, C., 2021. Dynamic interactions between
23 773 subduction zones. *Glob Planet Change* 202, 103501.
24 774 <https://doi.org/10.1016/J.GLOPLACHA.2021.103501>
25 775 Király, Á., Holt, A.F., Funicello, F., Faccenna, C., Capitanio, F.A., 2018. Modeling Slab-Slab
26 776 Interactions: Dynamics of Outward Dipping Double-Sided Subduction Systems.
27 777 *Geochemistry, Geophysics, Geosystems* 19, 693–714.
28 778 <https://doi.org/10.1002/2017GC007199>
29 779 Kohlstedt, D.L., Evans, B., Mackwell, S.J., 1995. Strength of the lithosphere: Constraints
30 780 imposed by laboratory experiments. *J Geophys Res Solid Earth* 100, 17587–17602.
31 781 <https://doi.org/10.1029/95JB01460>
32 782 Kufner, S.K., Schurr, B., Sippl, C., Yuan, X., Ratschbacher, L., Akbar, A. s/of M., Ischuk, A.,
33 783 Murodkulov, S., Schneider, F., Mechie, J., Tilmann, F., 2016. Deep India meets deep Asia:
34 784 Lithospheric indentation, delamination and break-off under Pamir and Hindu Kush (Central
35 785 Asia). *Earth Planet Sci Lett* 435, 171–184. <https://doi.org/10.1016/J.EPSL.2015.11.046>
36 786 Lamb, S., 2015. Kinematics to dynamics in the New Zealand Plate boundary zone: implications
37 787 for the strength of the lithosphere. *Geophys J Int* 201, 552–573.
38 788 <https://doi.org/10.1093/GJI/GGV027>
39 789 Lin, S.C., Kuo, B.Y., 2016. Dynamics of the opposite-verging subduction zones in the Taiwan
40 790 region: Insights from numerical models. *J Geophys Res Solid Earth* 121, 2174–2192.
41 791 <https://doi.org/10.1002/2015JB012784>
42 792 Maiti, G., Roy, A., Sen, J., Mandal, N., 2021. Impact of Decelerating India-Asia Convergence on
43 793 the Crustal Flow Kinematics in Tibet: An Insight From Scaled Laboratory Modeling.
44 794 *Geochemistry, Geophysics, Geosystems* 22, e2021GC009967.
45 795 <https://doi.org/10.1029/2021GC009967>
46 796 Mansour, J., Giordani, J., Moresi, L., Beucher, R., Kaluza, O., Velic, M., Farrington, R.,
47 797 Quenette, S., Beall, A., 2020. Underworld2: Python Geodynamics Modelling for Desktop,
48 798 HPC and Cloud. *J Open Source Softw* 5, 1797. <https://doi.org/10.21105/joss.01797>
49
50
51
52
53
54
55
56
57
58
59
60
61
62
63
64
65

- 1
2
3
4 799 Maunder, B., Prytulak, J., Goes, S., Reagan, M., 2020. Rapid subduction initiation and
5 800 magmatism in the Western Pacific driven by internal vertical forces. *Nature*
6 801 *Communications* 2020 11:1 11, 1–8. <https://doi.org/10.1038/s41467-020-15737-4>
7 802 Merkuriev, S.A., Sotchevanova, N.A., 2003. Structure and evolution of the Carlsberg Ridge:
8 803 Evidence for non-stationary spreading on old and modern spreading centres on JSTOR
9 804 [WWW Document]. *Curr Sci*. URL <https://www.jstor.org/stable/24108663> (accessed
10 805 11.8.23).
11 806 Miles, P.R., 1982. Gravity models of the Amirante Arc, western Indian Ocean. *Earth Planet Sci*
12 807 *Lett* 61, 127–135. [https://doi.org/10.1016/0012-821X\(82\)90045-0](https://doi.org/10.1016/0012-821X(82)90045-0)
13 808 Mishin, Y.A., Gerya, T. V., Burg, J.P., Connolly, J.A.D., 2008. Dynamics of double subduction:
14 809 Numerical modeling. *Physics of the Earth and Planetary Interiors* 171, 280–295.
15 810 <https://doi.org/10.1016/J.PEPI.2008.06.012>
16 811 Molnar, P., Stock, J.M., 2009. Slowing of India’s convergence with Eurasia since 20 Ma and its
17 812 implications for Tibetan mantle dynamics. *Tectonics*.
18 813 <https://doi.org/10.1029/2008TC002271>
19 814 Peral, M., Király, Á., Zlotnik, S., Funicello, F., Fernández, M., Faccenna, C., Vergés, J., 2018.
20 815 Opposite Subduction Polarity in Adjacent Plate Segments. *Tectonics* 37, 3285–3302.
21 816 <https://doi.org/10.1029/2017TC004896>
22 817 Peron-Pinvidic, G., Gernigon, L., Gaina, C., Ball, P., 2012. Insights from the Jan Mayen system
23 818 in the Norwegian–Greenland sea—I. Mapping of a microcontinent. *Geophys J Int* 191, 385–
24 819 412. <https://doi.org/10.1111/J.1365-246X.2012.05639.X>
25 820 Pusok, A.E., Stegman, D.R., 2020. The convergence history of India-Eurasia records multiple
26 821 subduction dynamics processes. *Sci Adv* 6.
27 822 https://doi.org/10.1126/SCIADV.AAZ8681/SUPPL_FILE/AAZ8681_SM.PDF
28 823 Pusok, A.E., Stegman, D.R., 2019. Formation and Stability of Same-Dip Double Subduction
29 824 Systems. *J Geophys Res Solid Earth* 124, 7387–7412.
30 825 <https://doi.org/10.1029/2018JB017027>
31 826 Sandiford, D., Moresi, L., 2019. Improving subduction interface implementation in dynamic
32 827 numerical models. *Solid Earth*. <https://doi.org/10.5194/se-10-969-2019>
33 828 Sengupta, S., Ray, K.K., Acharyya, S.K., de Smeth, J.B., 1990. Nature of ophiolite occurrences
34 829 along the eastern margin of the Indian plate and their tectonic significance. *Geology* 18,
35 830 439–442. [https://doi.org/10.1130/0091-7613\(1990\)018<0439:NOOOAT>2.3.CO;2](https://doi.org/10.1130/0091-7613(1990)018<0439:NOOOAT>2.3.CO;2)
36 831 Spiegelman, M., Katz, R.F., 2006. A semi-Lagrangian Crank-Nicolson algorithm for the
37 832 numerical solution of advection-diffusion problems. *Geochemistry, Geophysics,*
38 833 *Geosystems* 7. <https://doi.org/10.1029/2005GC001073>
39 834 Stern, R.J., 2004. Subduction initiation: spontaneous and induced. *Earth Planet Sci Lett* 226,
40 835 275–292. <https://doi.org/10.1016/J.EPSL.2004.08.007>
41 836 Stern, R.J., 2002. SUBDUCTION ZONES. *Reviews of Geophysics* 40, 3–1.
42 837 <https://doi.org/10.1029/2001RG000108>
43 838 Stevens, D.E., McNeill, L.C., Henstock, T.J., Delescluse, M., Chamot-Rooke, N., Bull, J.M.,
44 839 2020. A complete structural model and kinematic history for distributed deformation in the
45 840 Wharton Basin. *Earth Planet Sci Lett* 538, 116218.
46 841 <https://doi.org/10.1016/J.EPSL.2020.116218>
47 842 Tilling, R.I., 1996. Hazards and Climatic Impact of Subduction-Zone Volcanism: A Global and
48 843 Historical Perspective. *Geophysical Monograph Series* 96, 331–335.
49 844 <https://doi.org/10.1029/GM096P0331>
50
51
52
53
54
55
56
57
58
59
60
61
62
63
64
65

- 1
2
3
4 845 Van Der Voo, R., Spakman, W., Bijwaard, H., 1999. Tethyan subducted slabs under India. *Earth*
5 846 *Planet Sci Lett* 171, 7–20. [https://doi.org/10.1016/S0012-821X\(99\)00131-4](https://doi.org/10.1016/S0012-821X(99)00131-4)
6
7 847 Van Hinsbergen, D.J.J., Kapp, Paul, Dupont-Nivet, Guillaume, Lippert, Peter C, Decelles, Peter
8 848 G, Torsvik, Trond H, Hinsbergen, V., Kapp, P, Dupont-Nivet, G, Lippert, P C, Decelles, P G,
9 849 Torsvik, T H, 2011. Restoration of Cenozoic deformation in Asia and the size of Greater
10 850 India. *Tectonics* 30, 5003. <https://doi.org/10.1029/2011TC002908>
11 851 van Hunen, J., Allen, M.B., 2011. Continental collision and slab break-off: A comparison of 3-D
12 852 numerical models with observations. *Earth Planet Sci Lett* 302, 27–37.
13 853 <https://doi.org/10.1016/j.epsl.2010.11.035>
14 854 Vignaroli, G., Faccenna, C., Jolivet, L., Piromallo, C., Rossetti, F., 2008. Subduction polarity
15 855 reversal at the junction between the Western Alps and the Northern Apennines, Italy.
16 856 *Tectonophysics* 450, 34–50. <https://doi.org/10.1016/J.TECTO.2007.12.012>
17 857 Westerweel, J., Roperch, P., Licht, A., Dupont-Nivet, G., Win, Z., Poblete, F., Ruffet, G., Swe,
18 858 H.H., Thi, M.K., Aung, D.W., 2019. Burma Terrane part of the Trans-Tethyan arc during
19 859 collision with India according to palaeomagnetic data. *Nature Geoscience* 2019 12:10 12,
20 860 863–868. <https://doi.org/10.1038/s41561-019-0443-2>
21 861 Yang, S., Liang, X., Jiang, M., Chen, L., He, Y., Mon, C.T., Hou, G., Thant, M., Sein, K., Wan,
22 862 B., 2022. Slab remnants beneath the Myanmar terrane evidencing double subduction of the
23 863 Neo-Tethyan Ocean. *Sci Adv* 8, 1027.
24 864 https://doi.org/10.1126/SCIADV.ABO1027/SUPPL_FILE/SCIADV.ABO1027_SM.PDF
25 865 Yin, A., Harrison, T.M., 2000. Geologic Evolution of the Himalayan-Tibetan Orogen.
26 866 <https://doi.org/10.1146/annurev.earth.28.1.211> 28, 211–280.
27 867 <https://doi.org/10.1146/ANNUREV.EARTH.28.1.211>
28 868 Zhang, Q., Guo, F., Zhao, L., Wu, Y., 2017. Geodynamics of divergent double subduction: 3-D
29 869 numerical modeling of a Cenozoic example in the Molucca Sea region, Indonesia. *J*
30 870 *Geophys Res Solid Earth* 122, 3977–3998. <https://doi.org/10.1002/2017JB013991>
31 871 Zhou, X., Li, Z.H., Gerya, T. V., Stern, R.J., Xu, Z., Zhang, J., 2018. Subduction initiation
32 872 dynamics along a transform fault control trench curvature and ophiolite ages. *Geology* 46,
33 873 607–610. <https://doi.org/10.1130/G40154.1>
34 874 Zhu, M., Yan, Z., Pastor-Galán, D., Chen, L., Miao, L., Zhang, F., Li, S., Yang, S., 2023. Do
35 875 microcontinents nucleate subduction initiation? *Geology* 51, 668–672.
36 876 <https://doi.org/10.1130/G51222.1/5849054/G51222.PDF>
37 877
38
39
40
41
42
43
44
45
46
47
48
49
50
51
52
53
54
55
56
57
58
59
60
61
62
63
64
65

Declaration of Competing Interest

The authors declare that they have no known competing financial interests or personal relationships that could have appeared to influence the work reported in this article.

ACCEPTED MANUSCRIPT